Changes in Cross-Equatorial Ocean Heat Transport Impact Regional Climate and Precipitation Sensitivity

by

Oghenekevwe Christopher Oghenechovwen
B.Tech., The Federal University of Technology Akure, 2019

A Thesis Submitted in Partial Fulfillment of the
Requirements for the Degree of

MASTER OF SCIENCE

in the School of Earth and Ocean Sciences

© Oghenekevwe Christopher Oghenechovwen, 2022
University of Victoria

All rights reserved. This thesis may not be reproduced in whole or in part, by photocopying or other means, without the permission of the author.

Changes in Cross-Equatorial Ocean Heat Transport Impact Regional Climate and Precipitation Sensitivity

by

Oghenekevwe Christopher Oghenechovwen
B.Tech., The Federal University of Technology Akure, 2019

Supervisory Committee

Dr. Hansi Singh, Supervisor
(School of Earth and Ocean Sciences)

Dr. Adam Monahan, Departmental Member
(School of Earth and Ocean Sciences)

Dr. Ruby Leung, Outside Member
(Pacific Northwest National Laboratory)

ABSTRACT

Do changes in how cross-equatorial energy transport is partitioned between the ocean and atmosphere impact the hemispheric climate response to forcing? To find out, we alter the cross-equatorial ocean heat transport in a state-of-the-art GCM and ascertain how changes in energy transport and its partitioning impact hemispheric climate and precipitation sensitivity following abrupt CO_2-doubling. We further evaluate the applicability our results in CMIP6-class ESMs, where AMOC facilitates the northward cross-equatorial ocean heat transport. In our experiments, changes in ocean cross-equatorial energy transport trigger compensating changes in atmospheric energy transport through changes in the Hadley cells and a shift in the Intertropical Convergence Zone. However, the climate sensitivity in each hemisphere is linearly related to the ocean heat transport convergence, not atmospheric energy transport convergence, due to the impact of ocean heating on evaporation and atmospheric specific humidity. Similarly, we also find that ocean heat transport convergence controls the hemispheric precipitation sensitivity through the impact of ocean heating on surface evaporation. This relationship is also evident in CMIP6 models, where we find differences in hemispheric precipitation sensitivity to be related to the Atlantic Meridional Overturning Circulation (AMOC). Changes in the AMOC control hemispheric differences in upper ocean heat content, which then affect how the hydrologic cycle responds to CO_2 forcing in each hemisphere. These results suggest that ocean dynamics impact the hemispheric climate response to CO_2 forcing, particularly how much regional precipitation changes with warming.

Table of Contents

List of Tables

List of Figures

ACKNOWLEDGEMENTS

I would like to thank my advisor, Dr. Hansi Singh, for her training, mentorship, teaching, support, and advice. These helped me during my program and they will serve me well in the future. Dr. Singh also performed the slab ocean model experiments analyzed in this research. I am grateful for the guidance of my committee members, Dr. Adam Monahan and Dr. Ruby Leung, as well as Dr. John Fyfe who stepped down in my 2nd year.

I enjoyed my drop-in's at the Departmental office and the helpful chats with Dr. Jay Cullen (SEOS Director), Kalisa Valenzuela (Graduate Program Secretary), and Allison Rose (former Department Secretary). I also had a wonderful time with other students of the UVic Climate Dynamics Lab (especially Kyle Heyblom), the wider SEOS Climate Modelling Group (especially Camille Febvre, Ameneh Mollasharifi, Raj Deepak, and Yongxiao Liang), and SEOS (especially Parsa, Jia-Xuan, and Israporn).

I acknowledge additional funding awards from the Faculty of Graduate Studies and donors of the Dr. Arne H. Lane Graduate Fellowships in Marine Sciences and the Diana and Martin Hocking Graduate Scholarship. I thank the Earth System Grid Federation for archiving and providing access to the Coupled Model Intercomparison Project Phase 6 (CMIP6) data, which was essential for my research.

Thanks for sharing so much with me and being part of my journey: Dr. Francis Asuquo, Dr. Christian Buckingham, Dr. Akintomide Akinsanola, Dr. Stephen Ogungbenro, Dr. Adekunle Ajayi, and Ibukun Adewumi.

My gratitude also goes to my parents (Joseph and Victory), siblings (Ejiro, Tega, Ochuko, Efe, and Runor), and Pastor Victor Ayegba for their endless love, encouragement, support, humour and prayers. Through my program, I found warmth, strength, and community at the campus chapters of InterVarsity Christian Fellowship (thanks Alan, Terri, and the DeGreef's) and University Christian Ministry.

Finally, I would like to thank my friends, in BC and elsewhere, who are the best and have been a constant source of inspiration and cheer: Oluwabunmi "Bebe" Ayodele-Makun, Akinwale Akinro, Success Areeveso, Anne Joseph, Adeola Alle, Rufai Balogun, Adebowale Adebayo, Jephtah Uche, Simileoluwa Kafaru, Dennis Irorere, Bukola Jegede, and Bolarinwa Ajayi.

DEDICATION

God, my Father, who gives good and perfect gifts (James 1:17).

1: Introduction

The differential heating of the Earth's surface by the Sun creates an equator-to-pole temperature gradient in both hemispheres. Poleward transport of energy, a basic characteristic of the Earth's coupled climate system, counteracts this differential heating. The ocean contributes substantially to the total meridional energy transport, especially in the deep tropics where it dominates [Trenberth and Caron, 2001, Held, 2001, Wunsch, 2005]. Previous studies suggest that meridional ocean heat transport (OHT) warms the global mean climate by decreasing planetary albedo, due to reduced sea ice extent and low marine cloud cover, and by global atmospheric moistening [Winton, 2003, Herweijer et al., 2005, Barreiro et al., 2011, Rencurrel and Rose, 2018]. OHT also plays a role in modifying regional climate. For example, OHT maintains ice-free oceans like the Norwegian, Barents, and Labrador seas [Seager et al., 2002, Rhines et al., 2008] and potentially sustains northwest Europe's mild winter temperatures [Rhines et al., 2008, Yamamoto et al., 2015], however, this has been contested [for example, see Seager et al., 2002].

OHT generally tends to be poleward [Haar and Oort, 1973, Oort and Vonder Haar, 1976, Trenberth, 1979, Masuda, 1988, Carissimo et al., 1985], but in the Atlantic basin it is uniquely northward in both hemispheres due to the Atlantic Meridional Overturning Circulation [AMOC; Trenberth and Caron, 2001, Lumpkin and Speer, 2007, Trenberth and Fasullo, 2017, Forget and Ferreira, 2019]. The AMOC moves about 0.5 PW (10^{15} W) of heat across the equator, and then converges this in the North Atlantic [Marshall and Plumb, 2007, Buckley and Marshall, 2016, Klinger and Haine, 2019]. The northward cross-equatorial OHT by the AMOC (hereafter, X-OHT) is an important feature of the present-day climate. It modulates oceanic surface temperatures in the North Atlantic [Knight et al., 2005] and the maritime climate of northwest Europe [Vellinga and Wood, 2002, Jacob et al., 2005, Jackson et al., 2015], affects Arctic sea ice [Mahajan et al., 2011], and helps set the mean position of the Intertropical Convergence Zone [ITCZ; Kang et al., 2008, 2009, Frierson et al., 2013, Marshall et al., 2014, Moreno-Chamarro

et al., 2020]. Other studies suggest that the observed interhemispheric temperature asymmetry is also due to the X-OHT [Croll, 1870, Feulner et al., 2013, Marshall et al., 2014, Kang et al., 2015].

Both models and paleo-proxy evidence suggest that the AMOC may respond to greenhouse gas forcing [Broecker, 1997, Srokosz et al., 2012]. Increasing atmospheric concentrations of greenhouse gases may invoke changes in surface buoyancy fluxes that could lead to a decline of the AMOC, and therefore, its northward OHT. Weakening of the AMOC in response to continued anthropogenic forcing is evident in projections of the latest generation of Earth System Models (hereafter, ESMs) that contributed to the Coupled Model Intercomparison Project Phase 6 [CMIP6; Weijer et al., 2020]. AMOC weakening, following increased greenhouse gases, may drive global and regional climate impacts which could have far-reaching societal consequences. Vellinga and Wood [2008], Zickfeld et al. [2008], Kuhlbrodt et al. [2009], Lin et al. [2019], and Liu et al. [2020] find that the Northern Hemisphere (NH) generally warms less than the Southern Hemisphere (SH) with AMOC weakening in modelling studies, while Vellinga and Wood [2008] and Rugenstein et al. [2013] showed that this weakening also reduces warming over Europe and at high northern latitudes, respectively. Consistent with relative cooling of the NH, AMOC weakening in response to CO_2–forcing is also associated with less Arctic and sub-Arctic sea ice loss [Rugenstein et al., 2013, Liu et al., 2020]. Drijfhout et al. [2012] and Bellomo et al. [2021] suggest that the minimum sea surface warming in the subpolar North Atlantic, termed the warming hole, is related to the magnitude of future AMOC weakening. Projected changes in the Atlantic storm track [Woollings et al., 2012] and Atlantic sea level [Vellinga and Wood, 2008, Kuhlbrodt et al., 2009] also depend on the magnitude of changes in the AMOC. Furthermore, AMOC weakening drives drying over northwestern Europe [Vellinga and Wood, 2008] and also impacts the tropical large-scale precipitation response by influencing a southward displacement of the ITCZ from its climatological position [Liu et al., 2020, Bellomo et al., 2021]. Liu et al. [2020] and Bellomo et al. [2021] also argue that a weakened AMOC causes the midlatitude jet to strengthen and shift poleward.

A number of studies focusing on the climatic impact of AMOC decline in a warming world go beyond statistical analyses (e.g. regression) to explore independent causality, commonly through freshwater perturbations. Vellinga and Wood [2008] induced a mid-21st century AMOC shutdown in the Hadley Centre Coupled Model, version 3 through abrupt freshwater hosing of 5×10^5 km^3 in the North

Atlantic, with greenhouse gas concentrations rising according to an IS92a scenario [Leggett et al., 1992, Pepper, 1992]. Instead of freshwater hosing with a sudden onset and prescribed rate [as in Vellinga and Wood, 2008], the freshwater perturbation applied in Zickfeld et al. [2008] and Kuhlbrodt et al. [2009] under SRES emission scenarios [Nakicenovic and Swart, 2000] is proportional to the increase in NH surface air temperature in their respective models, the University of Victoria Earth System Climate Model and Climber-3α (both ESMs of intermediate complexity). Liu et al. [2020] held AMOC strength fixed through freshwater removal from the subpolar North Atlantic in historical and Representative Concentration Pathway 8.5 simulations with the Community Climate System Model version 4, and contrast this to another experiment with similar forcing but a freely evolving AMOC in order to isolate impacts.

However, this method of applying anomalous freshwater fluxes over the North Atlantic has some important limitations. By imposing AMOC changes in this manner, compensating ocean circulation changes in other basins may be triggered unintentionally. For example, the southward cross-equatorial ocean heat transport by the shallow meridional overturning circulation in the Indian basin [Trenberth and Caron, 2001, Trenberth and Fasullo, 2017, Forget and Ferreira, 2019] may be affected since the North Atlantic and Indian basins are teleconnected. Both are connected through the potential impacts of tropical hydrological cycle on Atlantic salinity and of surface winds on turbulent heat fluxes [Hu and Fedorov, 2019, 2020, McMonigal et al., 2022, Yang et al., 2022]. Imposed AMOC weakening by freshwater perturbations in this manner likely leads to cooler sea surface temperatures in the North Atlantic, that contributes to enhanced surface wind-driven evaporative cooling and strenghtening of the gyre circulation and therefore, the shallow overturning meridional circulation in the Indian basin. This implies that climate impacts presented in these freshwater perturbation studies are due to imposed AMOC weakening, as well as to compensating basin-scale ocean circulation changes in response to freshwater forcing. In this case, the climate response due to AMOC decline cannot be separated from the climate response due to ocean responses in adjacent basins.

Weakening of the AMOC is mainly associated with diminishing X-OHT. Given the important thermodynamic influence of X-OHT, the main question we seek to answer here is this: how do direct changes in X-OHT impact the regional climate and hydrologic cycle response to CO_2–forcing, especially outside of the deep tropics? We investigate this question in an idealized manner using an Earth System

Model (ESM) coupled to a slab ocean. With this framework, we vary X-OHT and simultaneously double the atmospheric concentration of CO_2 in order to determine independent impacts. Additionally, we employ energetics and radiative feedback analyses to mechanistically explain how X-OHT impact the regional climate response to CO_2 forcing in our sensitivity experiments. We go further and evaluate the applicability of our idealized results in CMIP6-class models, where AMOC decline of varying magnitudes is evident [Weijer et al., 2020]. This thesis is structured as follows. In Chapter 2, we describe our data, model experiments, and analyses. We present results in Chapter 3 on the AMOC, climate, and hydrologic response to CO_2-quadrupling in CMIP6. The AMOC response is found to have a strong statistical relationship with the hemispheric asymmetry in climate and hydrologic responses. These statistical relationships motivates Chapter 4, which is on the causal impact of varying X-OHT on the regional climate and the hydrologic cycle response in our idealized model framework. We find that atmospheric response efficiently compensates changes in X-OHT. In Chapter 4, we also evaluate the role of radiative feedbacks and energetics in the climate response and how X-OHT changes directly influence the hydrologic cycle. Chapter 5 is on the spatial pattern of AMOC impact on climate and the hydrologic cycle in CMIP6, as well as mechanisms underlying these impacts. Chapter 6 covers discussion on the implication of our results, concluding remarks, and future outlook.

2: Method

2.1. Analysis of CMIP6 Experiments

We use pre-industrial control (`piControl`) and abrupt atmospheric CO_2-quadrupling (`abrupt-4xCO2`) experiments from the Coupled Model Intercomparison Project Phase 6 [hereafter, CMIP6; Eyring et al., 2016] archive to evaluate relationships between the AMOC and surface climate. In CMIP6, `piControl` describes a simulation with conditions representative of the period before the onset of large-scale industrialization, with 1850 being the reference year. Meanwhile, `abrupt-4xCO2` describes a simulation with the concentration of atmospheric CO_2 instantaneously quadrupled from the annual mean 1850 value (from 284.3 ppm to 1137.2 ppm CO_2). The 24 CMIP6-class models analyzed had submitted at least 6 of 7 variables of interest to Earth System Grid Federation data nodes at the time of writing this thesis. For each CMIP6 model, the change or response in a variable is calculated as the difference between the annual mean of the final 30 years (years 120 to 150) of the `abrupt-4xCO2` simulation and the reference period, the annual mean of that model's equilibrated `piControl` simulation.

2.2. CESM1-SOM Experiments

The Community Earth System Model version 1 [CESM1; Hurrell et al., 2013] is coupled to a slab ocean model [SOM; Bitz et al., 2012] and then used to investigate the independent impact of varying cross-equatorial ocean heat transport (X-OHT) on the climate and hydrologic cycle response to CO_2 doubling. CESM1's components are the Community Atmosphere Model version 5 [CAM5; Neale et al., 2012] which has 30 vertical levels, Community Sea Ice CodE version 4 [CICE4; Hunke and Lipscomb, 2008], and the Community Land Model version 4 [CLM4; Oleson et al., 2010]. All model components are at a nominal horizontal resolution of 1°. As described in Bitz et al. [2012], the mixed layer temperature in our model configuration, hereafter CESM1-SOM, is governed by:

$$\rho_o c_p h_{mix} \frac{dT_{mix}}{dt} = F_{netsurface} + Q_{flux} \ , \tag{2.1}$$

where ρ_o is the density of ocean water (in Kg m^{-3}), c_p is the specific heat capacity of ocean water (in J kg^{-1} K^{-1}), h_{mix} is the spatially varying annual mean depth of the mixed layer (in m), T_{mix} is the ocean mixed-layer temperature (in K) and equals the sea surface temperature, $F_{netsurface}$is the net surface heat flux into the ocean (in W m^{-1}), and Q_{flux} is the prescribed ocean heat flux convergence (OHFC, or 'q flux') in the climatological ocean mixed layer (also in W m^{-1}). The OHFC represents the net effects of deepwater exchange and ocean heat transport (particularly in the zonal mean) usually through interactive ocean circulation. It can be determined from an existing monthly-mean climatological simulation (such as from an equilibrated, fully-coupled pre-industrial control run) or externally constructed in an idealized manner [see, e.g., Bitz et al., 2012, Rencurrel and Rose, 2018, Singh et al., 2022].

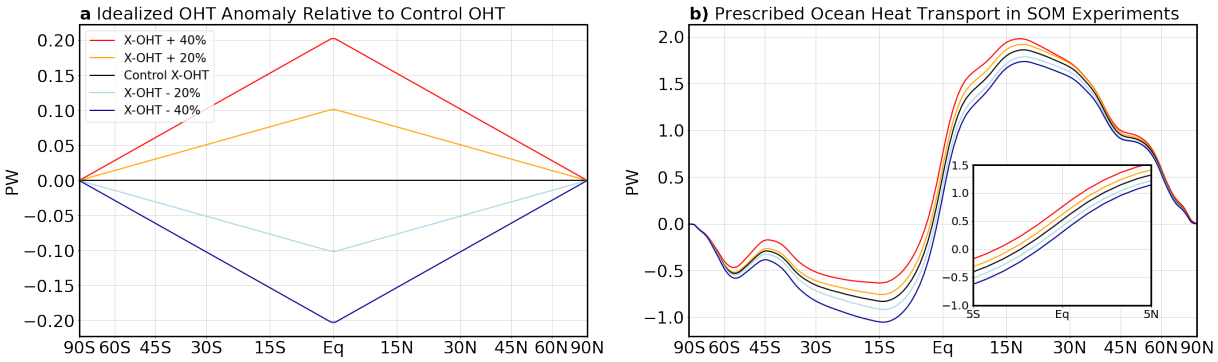

Figure 2.1.: (a) Idealized ocean heat transport (OHT) anomaly (in PW) relative to pre-industrial control simulation in CESM1-SOM experiments. (b) Prescribed OHT (in PW) in CO_2–doubling experiments. `X-OHT+40%` (red line) and `X-OHT+20%` (orange line) have prescribed X-OHT that is 40% and 20% greater in magnitude than `Control X-OHT` (black line), respectively; and `X-OHT-40%` (dark blue line) and `X-OHT-20%` (light blue line) have prescribed X-OHT that is 40% and 20% smaller in magnitude than `Control X-OHT`, respectively.

The CESM1-SOM experimental set-up is comprised of five abrupt CO_2-doubling simulations (`2xCO2`), each one with varying X-OHT, and a pre-industrial control simulation (`PI`). All experiments are 60 years long. The CESM1-SOM pre-industrial simulation (`PI`) is forced with prescribed monthly climatological ocean heat flux convergence (OHFC) that was derived from the fully-coupled CESM Large Ensemble (CESM1-LE) pre-industrial simulation [Kay et al., 2015]. At the

start of the `2xCO2` simulations, the concentration of atmospheric CO_2 is instantaneously doubled from the global annual mean pre-industrial value (from 284.3 ppm to 568.6 ppm CO_2).

To alter X-OHT and achieve differences between our CO_2-doubling simulations, we simultaneously adjust the climatological OHFC, over all latitudes and seasons, to be equal to one of the constructed spatial fields summarised in Table 2.1. In summary, we calculate 20% and 40% of the climatological X-OHT and scale these by ocean area of the Northern (NH) and Southern Hemispheres (SH) respectively. Here, scaling means that a quantity (% of climatological X-OHT) has been divided by some amount (hemispheric ocean area). The resulting NH scaled value is then added to the climatological OHFC over the NH, and the resulting SH scaled value is subtracted from the climatological OHFC over the SH to give a percentage (e.g. 20% or 40%) increase in X-OHT. Similarly, to obtain CO_2-doubling simulations with a simultaneous decrease in X-OHT, the resulting NH scaled value is then subtracted from the climatological OHFC over the NH, and the resulting SH scaled value is added to the climatological OHFC over the SH. We also ensure that the perturbation is greater in the NH due to its smaller ocean extent relative to the SH so the globally integrated OHFC is zero and the ocean-atmosphere mixed-layer system is in equilibrium.

Figure 2.1a shows the idealized OHT anomaly for our experiments relative to the CESM1-SOM pre-industrial control simulation `Control OHT`. `X-OHT+40%` (red line) and `X-OHT+20%` (orange line) have specified X-OHT that is larger than that in `Control X-OHT` by 40% and 20%, respectively. In contrast, specified X-OHT in `X-OHT-20%` (light blue line) and `X-OHT-40%` (dark blue line) are smaller in magnitude than `Control X-OHT` by 20% and 40%, respectively. In `Control X-OHT` (black line), X-OHT is not altered from the 1850s pre-industrial value, which is 0.5 PW. Figure 2.1b shows the prescribed ocean heat transport in our CO_2-doubling experiments, while the inset shows this only between 5°S and 5°N. As expected, OHT in the NH is larger in `X-OHT+40%` and `X-OHT+20%` than in `X-OHT-20%`, and `X-OHT-40%`. In the SH, OHT is greater in `X-OHT+40%` and `X-OHT+20%` than in `X-OHT-20%`, and `X-OHT-40%`. In the inset, we clearly see that X-OHT is greater in `X-OHT+40%` (red line) and `X-OHT+20%` (orange line) than in `Control X-OHT` (black line), `X-OHT-20%` (light blue line), and `X-OHT-40%` (dark blue line).

Climatologies are computed using the final 30 years of each CO_2-doubling experiment, when the experiments are in equilibrium (i.e. the net top-of-atmosphere imbalance is ≤ 0.1 W m^{-2}). For each experiment, the response to CO_2-doubling is

Table 2.1.: Experiments used in this study.

Experiment	CO_2–forcing	Monthly climatological OHFC construction	Simulation time
Pre-industrial control run	fixed 1850s CO_2 value	derived from CESM-LE pre-industrial run [Kay et al., 2015]	60 years
Pertubed runs	abrupt CO_2–doubling	changed relative to the pre-industrial control	60 years
`X-OHT+40%`	"	relatively amplified (reduced) by 40% in the NH (SH)	"
`X-OHT+20%`	"	relatively amplified (reduced) by 20% in the NH (SH)	"
`Control X-OHT`	"	relatively held equal	"
`X-OHT-20%`	"	relatively reduced (amplified) by 20% in the NH (SH)	"
`X-OHT-40%`	"	relatively reduced (amplified) by 20% in the NH (SH)	"

computed as the difference between the `2xCO2` climatology and the pre-industrial control CESM1-SOM simulation.

3: The CO_2–quadrupling Response in CMIP6

3.1. The Atlantic Meridional Overturning Circulation Response

The CMIP6 archive [Eyring et al., 2016] allows us to directly compare the climate and hydrologic cycle response to CO_2-quadrupling across the latest generation of fully coupled ESMs. First, we assess the intermodel range in how the AMOC responds to CO_2-quadrupling in 24 CMIP6-class ESMs (Fig. 3.1a). Unless otherwise specified, AMOC strength in this thesis is defined as the maximum strength of the annual mean overturning stream function between 400m and 2000m in the North Atlantic basin. All ESMs evaluated exhibit a decline in maximum strength of the AMOC with CO_2-quadrupling [Weijer et al., 2020], but the range of this decline varies widely: from -3.2Sv in INM-CM5-0 to -21.8Sv in CESM2-WACCM-FV2. If the magnitude of the decline in the AMOC approximates its pre-industrial strength, we infer an AMOC collapse in that ESM. The CESM2, CNRM, and the MIROC family of models, as well as MRI-ESM2-0, experience an AMOC collapse with CO_2-quadrupling based on this definition (analysis not presented here). While the Working Group I contribution to the Intergovernmental Panel on Climate Change's Sixth Assessment Report notes that CMIP6 models do not display an AMOC collapse in the 21st century under socioeconomic-based emissions scenarios [IPCC, 2021], these results suggest that an AMOC collapse is more plausible with larger forcings, like an instantaneous quadrupling of atmospheric CO_2 (`abrupt-4xCO2`).

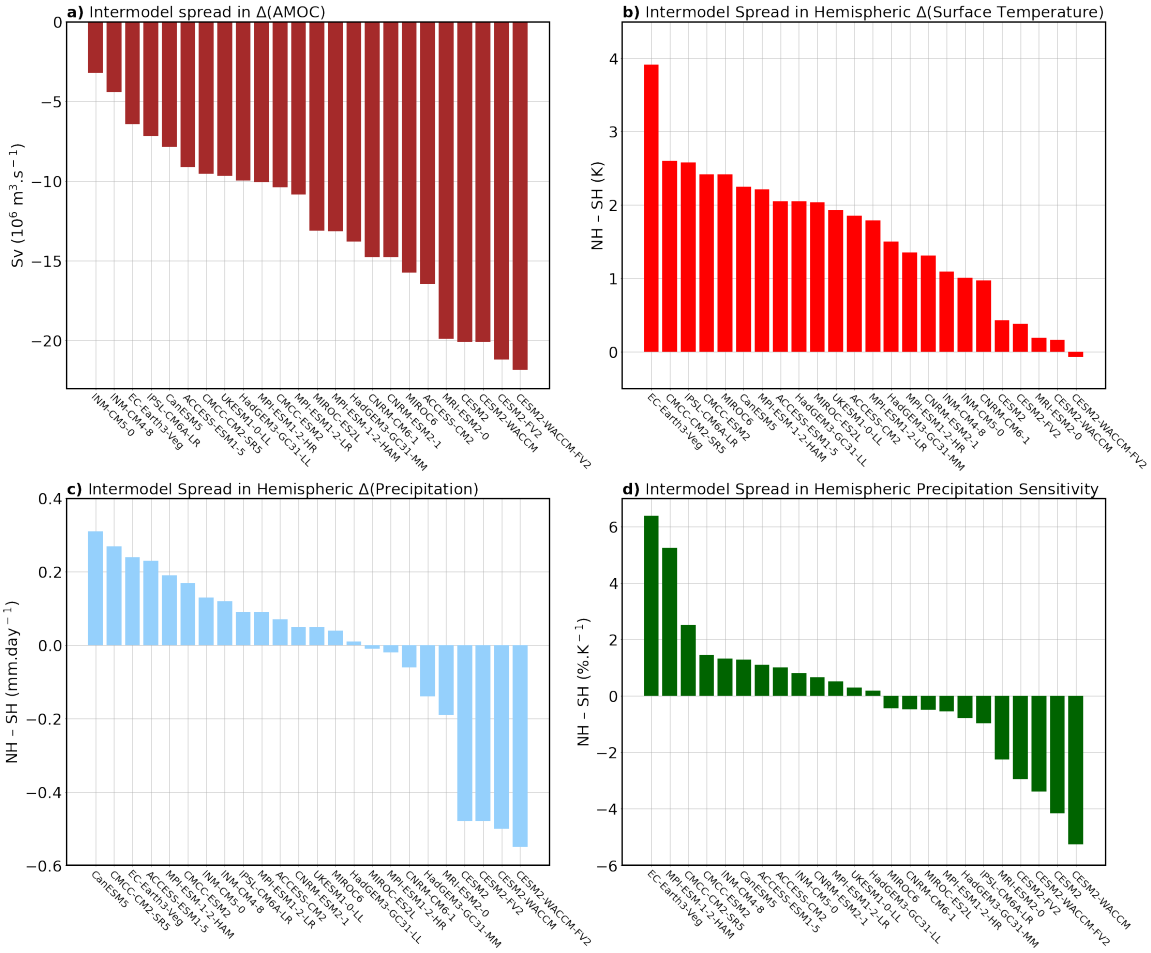

Figure 3.1.: a) Change in the maximum strength of the Atlantic Meridional Overturning Circulation (AMOC; in Sv). Intermodel spread in hemispheric difference (Northern hemisphere minus Southern hemisphere) in b) near-surface temperature change (in K); c) precipitation change (in mm/day) and d) precipitation sensitivity (in %/K). Calculated over years 120-150 of `abrupt-4xCO2`, relative to `piControl`, for 24 global climate models that contributed simulations to CMIP6.

3.2. Hemispheric Asymmetry in Climate and Hydrologic Cycle Response

We next assess the intermodel range in the hemispheric surface temperature and precipitation response to CO_2–quadrupling (Fig. 3.1b-d). To do this, we calculate the hemispheric asymmetry (the North Hemisphere, NH, average minus the South Hemisphere, SH, average) in warming and precipitation response in each ESM. Nearly all ESMs (23 out of 24 investigated) show greater surface warming in the NH than in the SH with CO_2-quadrupling, with warming in the NH exceeding that in the SH by up to 4K (Fig. 3.1b). On the other hand, more than half of the ESMs show greater precipitation increase in the NH than the SH (Fig. 3.1c). The intermodel range of asymmetry in precipitation change between hemispheres is 0.86 mm/day. Here, we define hemispheric precipitation sensitivity as the percentage change in hemispheric precipitation per unit degree of hemispheric warming. About half of the ESMs have higher precipitation sensitivity in the NH than in the SH (Fig. 3.1d). The intermodel range of asymmetry in precipitation sensitivity between hemispheres is 11.63%/K.

3.3. Relationship Between AMOC Changes and Climate and Precipitation Response

Previous studies suggest that AMOC changes may impact the hemispheric climate response [see Vellinga and Wood, 2008, Zickfeld et al., 2008, Kuhlbrodt et al., 2009, Rugenstein et al., 2013, Lin et al., 2019, Liu et al., 2020, Bellomo et al., 2021]. Among CMIP6-participating models, we see a statistically significant linear relationship between AMOC decline and the hemispheric asymmetry in surface warming ($r = 0.64$, $p < 0.01$; Fig. 3.2a). ESMs with stronger AMOC decline tend to display comparable warming between the NH and SH, consistent with previous findings in ESMs from CMIP5 [Lin et al., 2019]. On the other, in ESMs with a weaker AMOC decline, the NH tends to warm more than the SH. In Figure 3.2b, we also see a statistically significant relationship between AMOC decline and hemispheric difference in precipitation change ($r = 0.82$, $p < 0.01$). ESMs with stronger AMOC decline generally exhibit greater precipitation increase in the SH than in the NH, while ESMs with weaker AMOC decline show greater precipitation increase in the NH than in the SH. Similarly, as shown in Figure 3.2c, there is a statistically significant relationship between AMOC decline and

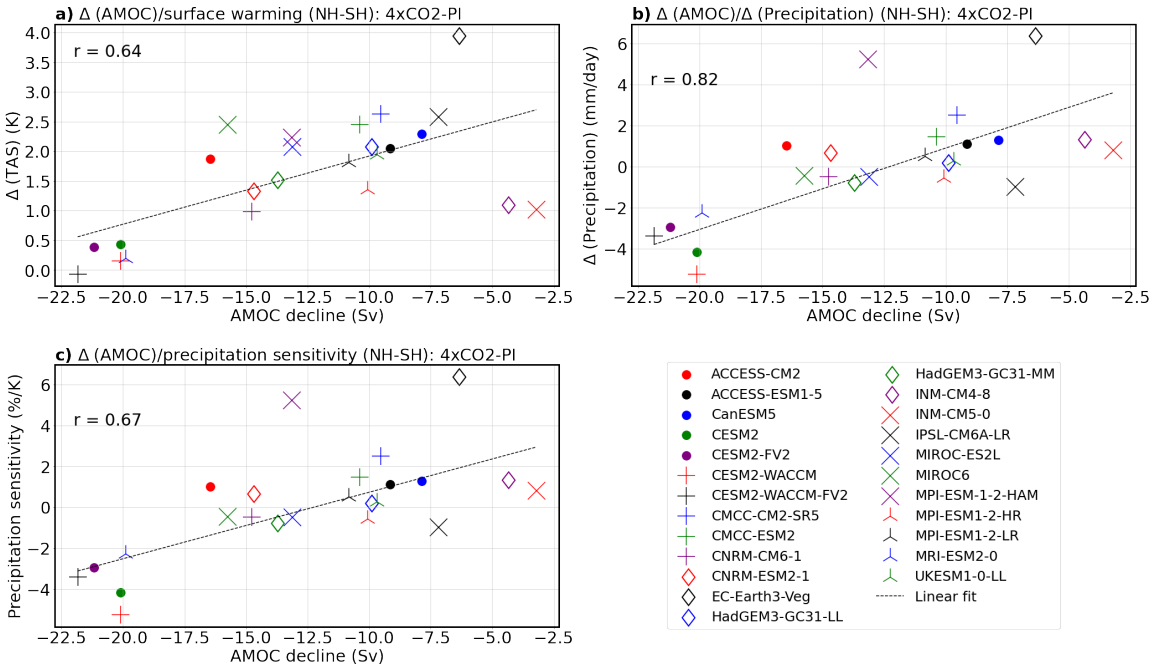

Figure 3.2.: Relationship between the hemispheric difference (Northern hemisphere minus Southern hemisphere) in a) surface temperature change (in K); b) precipitation change (in mm/day); and c) precipitation sensitivity (in %/K) with CO_2-quadrupling and change in the maximum strength of the Atlantic Meridional Overturning Circulation (AMOC; in Sv). Calculated over years 120-150 of `abrupt-4xCO2`, relative to `piControl`, for 24 global climate models that contributed simulations to CMIP6. Correlations are statistically significant at $p < 0.01$.

hemispheric difference in precipitation sensitivity ($r = 0.67$, $p < 0.01$). In ESMs with greater AMOC decline, precipitation sensitivity tends to be greater in the SH than in the NH. Conversely, in ESMs with weaker AMOC decline, precipitation sensitivity is greater in the NH than in the SH.

4: CO_2–doubling Response with Idealized Changes in X-OHT

Here, we present results from CESM1-SOM (see Chapter 2) on the impact of X-OHT changes on the climate and the hydrologic cycle response to CO_2-doubling in and outside the deep tropics. AMOC weakening drives diminishing X-OHT in the coupled climate system. Modelling studies with ESMs that rely on freshwater perturbations to enforce AMOC weakening could unintentionally set up compensating basin-scale ocean circulation responses, e.g. in the Indian Ocean basin [Hu and Fedorov, 2019, 2020, McMonigal et al., 2022, Yang et al., 2022], that could affect the overall climate response to CO_2–forcing and make it difficult to independently evaluate the response due to forcing. To understand how changes in X-OHT independently impact the climate system response to CO_2-doubling, we analyze results from 5 CESM1-SOM experiments where we systematically perturb X-OHT while doubling atmospheric CO_2. Experimental design and setup are described further in Chapter 2.

4.1. Climate and Hydrologic Cycle Response Between Experiments with Idealized Changes in X-OHT

In Figure 4.1, we find that differences in X-OHT between CESM1-SOM experiments lead to sizeable differences in how temperature and precipitation respond to CO_2 doubling, even outside the deep tropics. Surface warming differs over most latitudes, and is particularly sizeable in the SH (Fig 4.1a; the range between experiments in the SH is 0.95K and it is 0.48K in the NH). In the SH, experiments with decreased X-OHT (`X-OHT-20%` and `X-OHT-40%`) experience greater warming than experiments with increased X-OHT (`X-OHT+20%` and `X-OHT+40%`). Conversely in the NH, experiments with decreased X-OHT (`X-OHT-20%` and `X-OHT-40%`) expe-

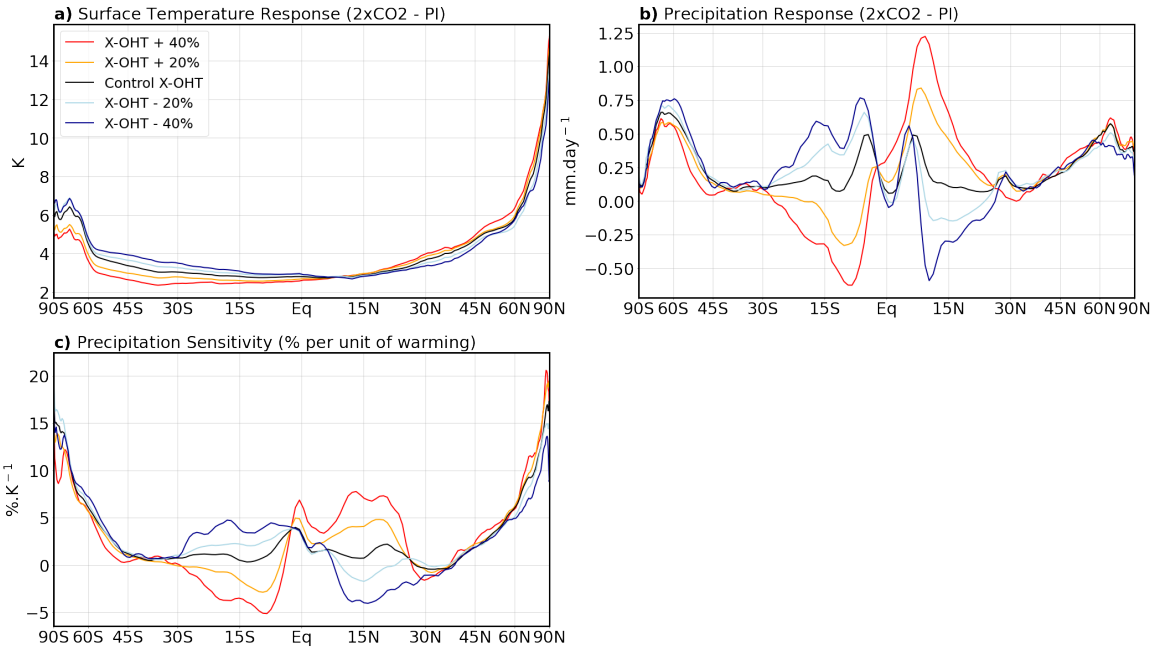

Figure 4.1.: (a) Zonal mean change in surface temperature (in K); (b) zonal mean change in precipitation (in mm/day) and c) zonal mean of precipitation sensitivity (in %/K).

rience lesser warming than experiments with increased X-OHT (`X-OHT+20%` and `X-OHT+40%`). Meanwhile, the difference in the precipitation response is greatest in the tropics of both hemispheres, but is also evident between 60N to 90N in the NH, and 45S to 65S in the SH (Fig 4.1b). Generally, `X-OHT+20%` and `X-OHT+40%` show greater precipitation increase in the NH than the SH when compared with `X-OHT-20%` and `X-OHT-40%`. The difference in precipitation sensitivity between experiments is greatest in the tropics (30S to 30N), and is also evident poleward of 45°in both hemispheres (Fig 4.1c; note that precipitation sensitivity is defined as the percentage change in local precipitation per degree of global warming in that experiment). In the SH, `X-OHT-20%` and `X-OHT-40%` generally show higher sensitivity than `X-OHT+20%` and `X-OHT+40%`. Conversely in the NH, `X-OHT-20%` and `X-OHT-40%` generally show smaller sensitivity than `X-OHT+20%` and `X-OHT+40%`.

Figure 4.2 shows the spatial pattern of surface warming in the CESM1-SOM CO_2-doubling experiments. We find that surface warming is greater in the NH when X-OHT increases (Figs 4.2a,b) and weaker when X-OHT decreases (Figs 4.2d,e). In contrast, SH warming is weaker when X-OHT increases (Figs 4.2a,b) and stronger when X-OHT decreases (Figs 4.2d,e). Furthermore, we find that NH warming in `X-OHT+20%` and `X-OHT+40%` exceeds `Control X-OHT` in most NH regions, but SH warming is weaker than that in `Control X-OHT` (Fig. 4.2f,g). On

the other hand, NH warming in `X-OHT-20%` and `X-OHT-40%` is weaker than `Control X-OHT` over most parts of the NH, but warming in most SH areas is greater than that in `Control X-OHT` (Fig. 4.2i,j).

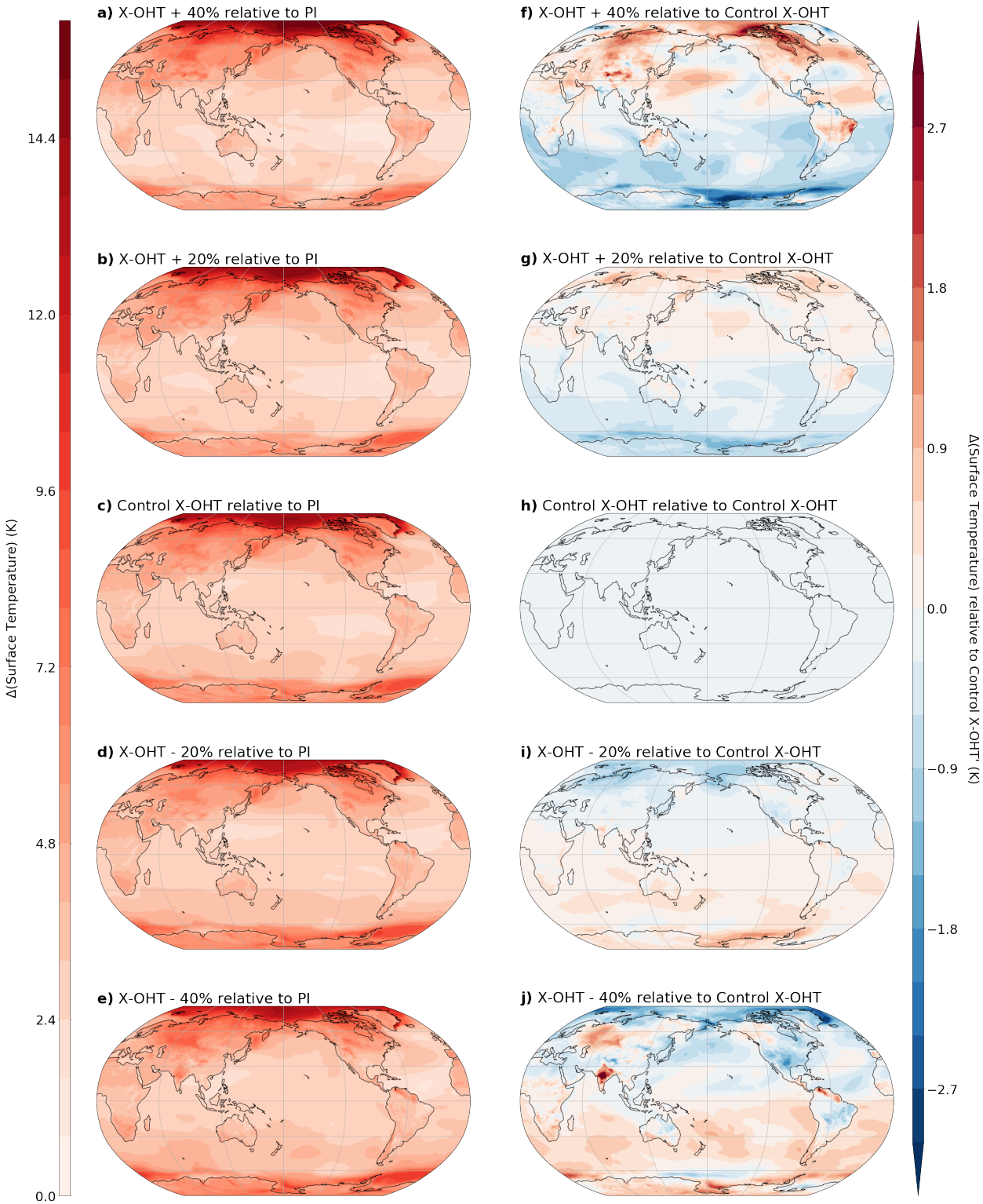

Figure 4.2.: Change in surface temperature (K) in the CESM1-SOM CO_2-doubling experiments, (a-e) relative to `PI`, and (f-j) relative to `Control X-OHT`.

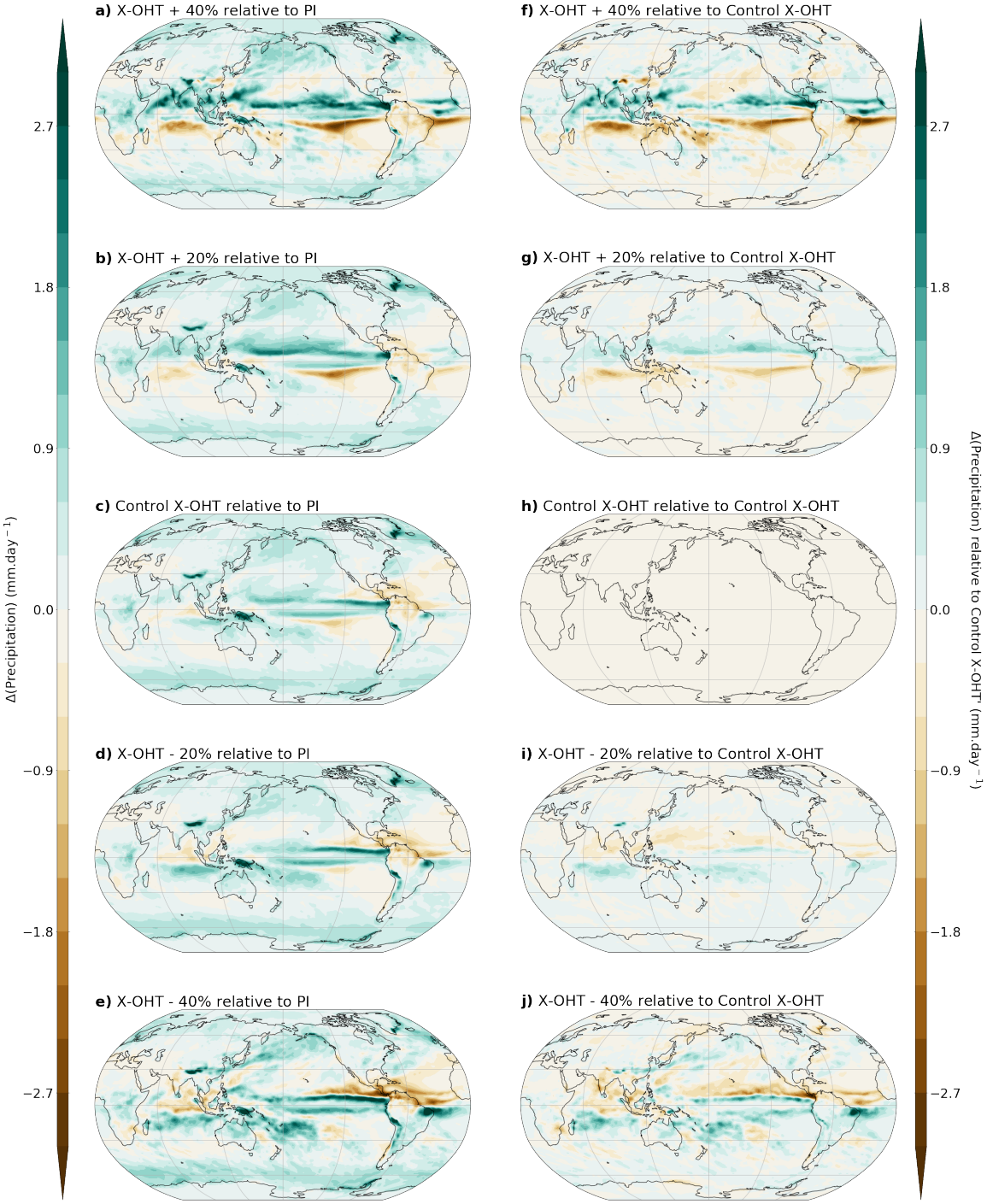

Figure 4.3.: Change in precipitation (mm/day) in the CESM1-SOM CO_2-doubling experiments, (a-e) relative to `PI` and (f-j) relative to `Control X-OHT`

.

Figure 4.3 shows the spatial pattern of precipitation changes across our experiments. The tropical precipitation maximum increases north of the equator with increasing X-OHT (`X-OHT+20%` and `X-OHT+40%` in Fig 4.3a,b) and increases south of the equator with decreasing X-OHT (`X-OHT-20%` and `X-OHT-40%` in Fig 4.3d,e). There is a greater increase in precipitation in most parts of the NH than SH with increasing X-OHT, especially at high-latitudes (Fig 4.3a,b). Conversely with decreasing X-OHT, precipitation in most SH latitudes increases more than similar NH latitudes (Fig 4.3c,d). Indeed, the precipitation response in `X-OHT+20%` and `X-OHT+40%` exceeds `Control X-OHT` in most parts of the NH, and is generally weaker than `Control X-OHT` in the SH (Fig. 4.3f,g). Conversely, the precipitation response in `X-OHT-20%` and `X-OHT-40%` is weaker than `Control X-OHT` over most parts of the NH, except over the storm track region, and is greater than `Control X-OHT` in most SH areas (Fig. 4.3i,j).

4.2. Energy Transport Response and Compensation

These results show that climate and hydrologic cycle responses are sensitive to changes in X-OHT, even outside the deep tropics. Figure 4.4 show energy transport changes with CO_2-doubling in each of the CESM1-SOM experiments. The pattern of OHT response is expected from experimental design (compare Fig 2.1 to Fig 4.4a), with `X-OHT+20%` and `X-OHT+40%` experiments having increased X-OHT relative to the pre-industrial control, as well as weaker poleward OHT in the SH and greater poleward OHT in the NH. Meanwhile, `X-OHT-20%` and `X-OHT-40%` experiments have reduced X-OHT, greater poleward OHT in the SH, and weaker poleward OHT in the NH. The atmospheric energy transport (AET) response to CO_2-doubling efficiently opposes the prescribed OHT changes (Fig 4.4b). Experiments with increased X-OHT (`X-OHT+20%` and `X-OHT+40%` in Fig 4.4b) exhibit a NH decrease in poleward AET, increase in the southward cross-equatorial AET, and a SH increase in poleward AET. On the other hand, experiments with reduced X-OHT (`X-OHT-20%` and `X-OHT-40%` in 4.4b) show a NH increase in poleward AET, decrease in the southward cross-equatorial AET, and a SH decrease in poleward AET. In the `Control X-OHT` experiment, the AET response to CO_2-doubling is small because there is no prescribed OHT anomaly to oppose. Previous studies have shown that OHT changes often lead to a compensating AET response [Bjerknes, 1964, Shaffrey and Sutton, 2006, Farneti and Vallis, 2013, Yang et al., 2015].

Because of the efficient compensation between prescribed OHT changes and the AET response, the Total Energy Transport (TET) response is generally small across experiments (Fig 4.4c). This result is reminiscent of that of Stone [1978], who showed that the negative relationship between AET and OHT is a fundamental feature of the coupled climate system and that TET (defined here as AET plus prescribed OHT) is set by the planetary albedo and astronomical parameters. TET is not overly sensitive to variations in atmospheric and oceanic processes that impact the transport mechanism [Stone, 1978]. Here, we also find that prescribed anomalies in X-OHT trigger efficient compensating responses in AET. Nevertheless, compensation between OHT and AET is imperfect. In the deep tropics (13S to 15N) for example, we observe that TET response is larger in `X-OHT-20%` and `X-OHT-40%` experiments (blue-hued lines in Fig 4.4c) in comparison to `X-OHT+20%` and `X-OHT+40%` experiments (red-hued lines). Outside the deep tropics, AET responses more effectively compensate for increasing X-OHT (i.e., red-hued lines lie closer to 0 in Fig 4.4c) than for decreasing X-OHT.

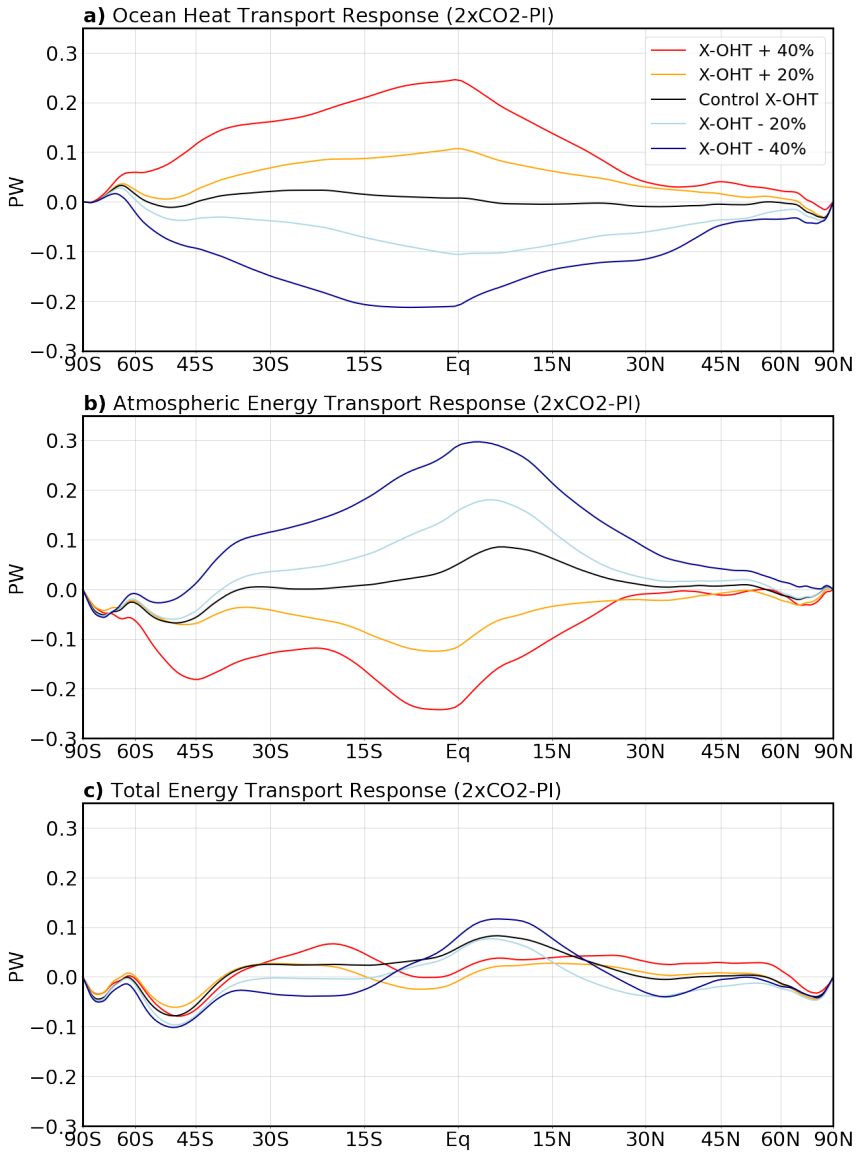

Figure 4.4.: Changes in energy transport: (a) the ocean heat transport anomaly (in PW); (b) the atmospheric energy transport response (in PW); and (c) the total energy transport response (in PW). Calculated over years 20-50 of `2xCO2`, relative to `PI`.

4.3. Role of Radiative Feedbacks and Energetics in the Climate Response

We now evaluate local radiative feedbacks and energetics in order to better understand how (prescribed) changes in X-OHT lead to differences in the hemispheric climate and hydrologic cycle response to CO_2-doubling across the CESM1-SOM experiments. Planck, lapse rate, water vapour, surface albedo, and cloud feedbacks (see Figs 4.6a-e) are estimated using the radiative kernel method [Soden et al., 2008, Shell et al., 2008], with kernels computed from CAM5 [Pendergrass et al., 2018]. These kernels quantitatively describe the net top-of-atmosphere radiation changes resulting from incremental changes in feedback variables (e.g. water vapour). We calculate local feedbacks by multiplying the radiative kernels by the change in feedback variables, and then normalizing by the local temperature change; this method assumes that the local net top-of-atmosphere radiation change is proportional to local surface warming [Feldl and Roe, 2013a,b].

In Figure 4.5, we show local surface warming contributions due to the sum of all local feedbacks, greenhouse gas forcing, and changes in energy transport convergence. We derive this by, first, decomposing the zonal mean energetic anomaly due to CO_2-doubling into components due to sum of feedbacks, forcing, and changes in energy transport convergence following expressions detailed in [Feldl and Roe, 2013b, Goosse et al., 2018, Singh et al., 2022]. This zonal mean energetic anomaly is expressed as

$$R_F(\theta) = \sum_i \lambda_i(\theta)\Delta T(\theta) - \Delta(\nabla \cdot F_{atm}(\theta)) - \Delta(\nabla \cdot F_{ocn}(\theta)) \ , \tag{4.1}$$

where each term is a function of latitude, θ. $R_F(\theta)$ is the zonal mean radiative forcing, $\lambda_i(\theta)$ is the i-th local feedback variable (Planck, lapse rate, water vapour, surface albedo, or cloud feedbacks), $\Delta T(\theta)$ is the zonal mean surface warming, $-\nabla \cdot F_{atm}(\theta)$ is the atmospheric energy transport convergence, and $-\nabla \cdot F_{ocn}(\theta)$ is the ocean heat transport convergence.

Meanwhile, the product $\lambda_i(\theta)\Delta T(\theta)$ is the change in top-of-atmosphere net radiation due to feedback variables. This can be expanded to show the top-of-atmosphere anomaly due to each of the local feedback variables λ_i:

$$\sum_i \lambda_i(\theta)\Delta T(\theta) = (\lambda_{Pl} + \lambda_{LR} + \lambda_{WV} + \lambda_{Al} + \lambda_{Cl})\Delta T \ , \tag{4.2}$$

where λ_{Pl} is the Planck feedback, λ_{LR} is the lapse rate feedback, λ_{WV} is the total water vapour feedback (longwave and shortwave components), λ_{Al} is the surface albedo feedback, and λ_{Cl} is the total cloud feedback (longwave and shortwave components).

We next split the Planck feedback, λ_{Pl} into a global mean component, $\overline{\lambda_{Pl}}$, and the spatial deviation from the global mean, λ'_{Pl}:

$$\lambda_{Pl} = \overline{\lambda_{Pl}} + \lambda'_{Pl} \ . \tag{4.3}$$

The global mean Planck feedback component, $\overline{\lambda_{Pl}}$, is the reference feedback variable in the climate system about which other feedbacks operate, i.e. the top-of-atmosphere energy loss per unit warming of the surface and troposphere in the absence of other feedbacks. Finally, we use equations (4.3), (4.2), and (4.1) to determine the local surface warming contributions, ΔT, due to the sum of all local feedbacks, greenhouse gas forcing, and changes in energy transport convergence [Feldl and Roe, 2013b, Goosse et al., 2018]:

$$\Delta T = -\frac{(\lambda'_{Pl} + \lambda_{LR} + \lambda_{WV} + \lambda_{Cl} + \lambda_{Al})\Delta T}{\overline{\lambda_{Pl}}} - \frac{R_f}{\overline{\lambda_{Pl}}} - \frac{\Delta(\nabla \cdot F_{atm})}{\overline{\lambda_{Pl}}} - \frac{\Delta(\nabla \cdot F_{ocn})}{\overline{\lambda_{Pl}}} \tag{4.4}$$

Figure 4.5a (same as Fig. 4.1a) shows the zonal mean temperature response to CO_2-doubling in the CESM1-SOM experiments. In the NH, warming is greater in experiments with increases in X-OHT (red-hued lines) compared to experiments with decreases in X-OHT (blue-hued lines). In the SH, experiments with decreases in X-OHT (blue-hued lines) display greater warming than experiments with increases in X-OHT (red-hued lines). There are also differences in how the sum of all radiative feedbacks contributes to surface warming between experiments (Fig. 4.5b). In experiments with increases in X-OHT (red-hued lines), the total feedback contributes more to local surface warming at nearly all latitudes in the NH and less in the SH, compared to experiments with decreases in X-OHT (blue-hued lines). Atmospheric CO_2-forcing is the same between experiments, so it does not contribute to differences in warming (Fig. 4.5c). The temperature contributions due to atmospheric energy transport convergence (AETC) and ocean heat transport convergence (OHTC) are small and are opposite between hemispheres (Fig. 4.5d,e). The temperature change due to AETC is more positive in the NH in experiments with decreases in X-OHT (blue-hued lines) and less positive in the SH (Fig. 4.5d). In contrast, the temperature change due to OHTC is less positive

in the NH in experiments with decreases in X-OHT (blue-hued lines) and more positive in the SH (Fig. 4.5e). As expected, the difference in temperature change due to total energy transport convergence (TETC) between experiments is small ($\sim$1K) and only distinguishable in the tropics (Fig. 4.5f). We therefore note that differences in the radiative feedbacks contribute the most to the differences in warming between experiments at nearly all latitudes. Figure 4.5g shows the sum of the temperature change due to feedbacks, forcing, and TETC. It resembles the actual zonal mean temperature change between experiments (Fig. 4.5a), and as indicated by the residual (difference between both), only slightly deviates at polar latitudes and the deep tropics (Fig. 4.5h).

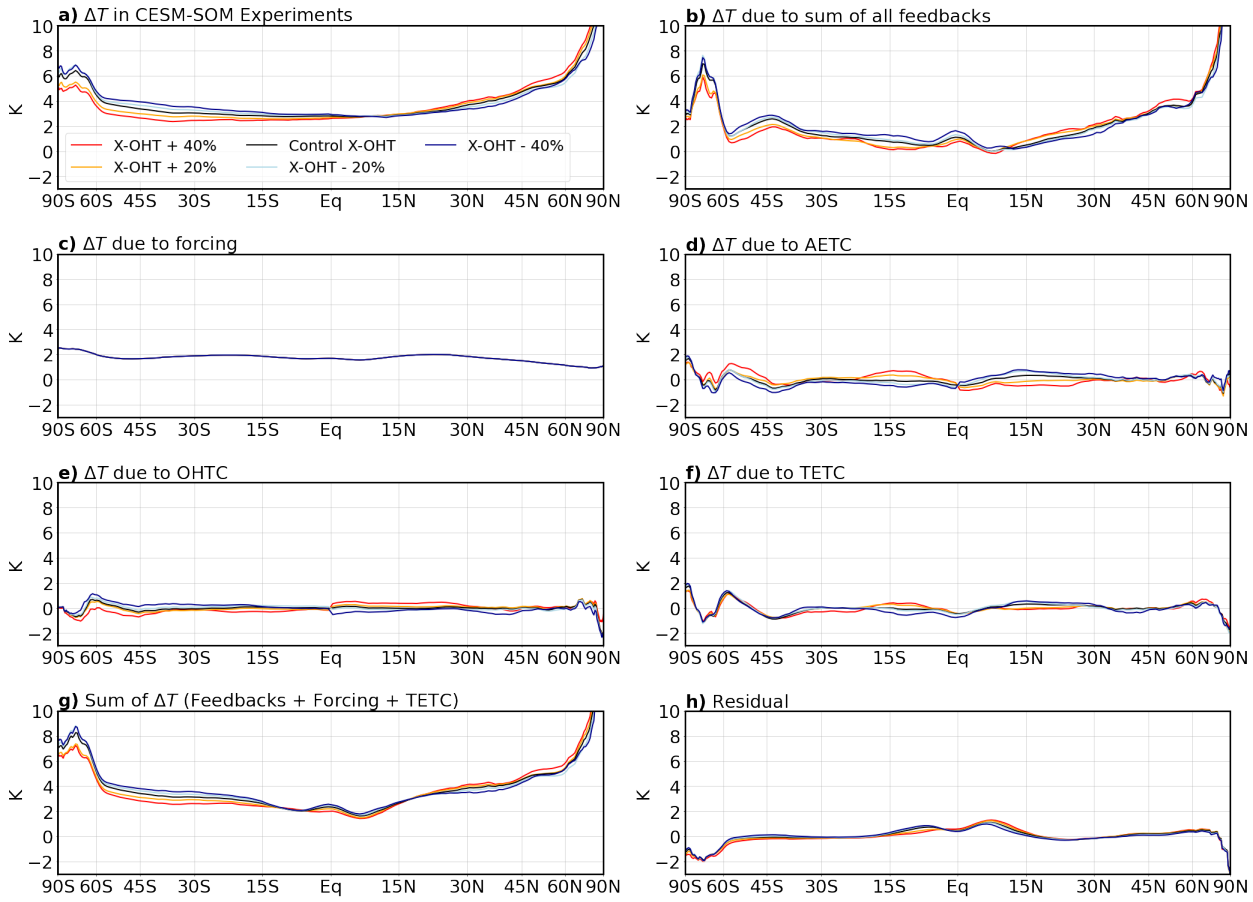

Figure 4.5.: Feedback, forcing, and energy transport contributions to the zonal mean temperature change (in K) in the CESM1-SOM CO_2-doubling experiments: (a) zonal mean temperature change; (b) temperature change attributable to the sum of radiative feedbacks; (c) temperature change attributable to the forcing (in the absence of radiative feedbacks); (d) temperature change due to changes in the atmospheric energy transport convergence; (e) temperature change due to (prescribed) changes in ocean heat transport convergence; (f) temperature change due to changes in the total energy transport convergence; (g) sum of temperature change contributions from the feedbacks, forcing, and total energy transport convergence; and (h) the residual of the decomposition, i.e. the difference between (a) and (g).

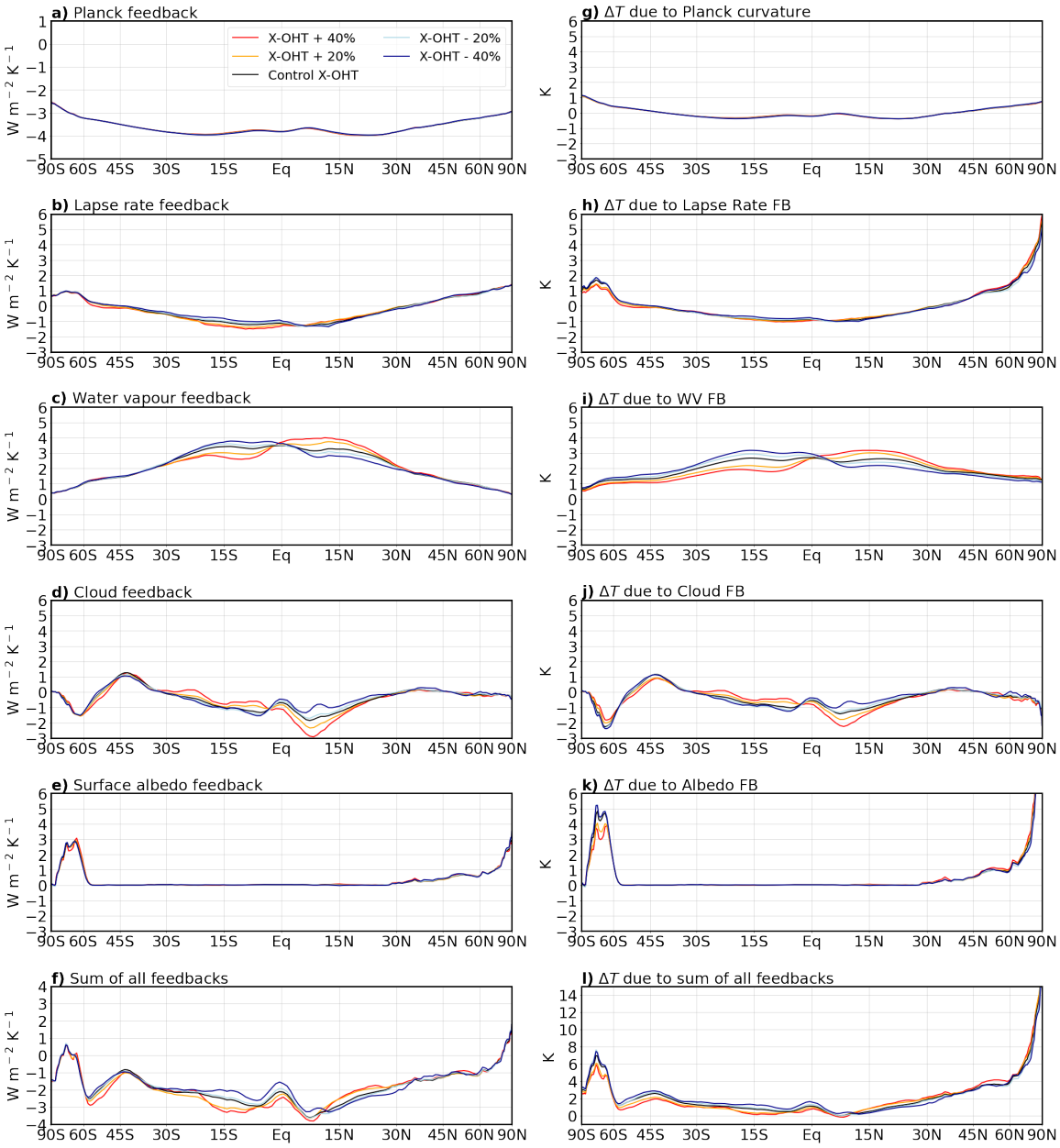

Figure 4.6.: Zonal mean local radiative feedbacks and temperature changes attributable to these radiative feedbacks in the CESM1-SOM CO_2-doubling experiments: (a-e) Plank, lapse rate, water vapour, cloud, and surface albedo radiative feedbacks (in W m^{-2} K^{-1}); (f) sum of radiative feedbacks (in W m^{-2} K^{-1}); and (g-k) temperature changes attributable to the Planck curvature, lapse rate feedback, water vapour feedback, cloud feedback, and surface albedo feedback (in K); and (l) total temperature change attributable to the radiative feedbacks (in K).

.

Since differences in the total radiative feedbacks contribute more than forcing and energy transport to the differences in warming between experiments at nearly all latitudes, we next evaluate independent feedback variables to understand their relative importance. Figures 4.6(a-e) show the Planck, lapse rate, total water vapour, surface albedo, and total cloud feedbacks. We see differences in the magnitude and pattern of zonal means of the radiative feedbacks between experiments (Figs 4.6a-e). These differences contribute to differences in the sum of all feedbacks across experiments (Fig 4.6f), which are noticeable in the tropics and between 45S-60S. The total feedback (sum of Planck, lapse rate, total water vapour, surface albedo, and total cloud feedbacks) in the SH is more stabilizing (more negative) when X-OHT increases, compared to when X-OHT decreases (as in `X-OHT-20%` and `X-OHT-40%`). Therefore, `X-OHT-20%` and `X-OHT-40%` experience greater SH warming than `X-OHT+20%` and `X-OHT+40%`. In the NH, in contrast, the total feedback is less stabilizing (less negative) when X-OHT increases (as in `X-OHT-20%` and `X-OHT-40%`) than when X-OHT decreases (`X-OHT-20%` and `X-OHT-40%`). This difference in radiative feedback between experiments is also consistent with difference in hemispheric warming, where `X-OHT+20%` and `X-OHT+40%` display more NH warming than `X-OHT-20%` and `X-OHT-40%`.

Figures 4.6(g-i) show the zonal surface warming attributable to the Planck curvature, lapse rate feedback, water vapour feedback, cloud feedback, and surface albedo feedback. We note that differences in zonal mean surface warming between experiments are due to water vapor at nearly all latitudes (Fig 4.6i), which increase the range of warming between experiments: the water vapour feedback amplifies warming in the NH in experiments where X-OHT increases, and amplifies warming in the SH in experiments where X-OHT decreases. Tropical clouds and clouds over the Southern Ocean region (45S-60S) are also important, but they decrease the range of warming between experiments: unlike the water vapour feedback, the cloud feedback in these regions amplifies warming in the NH in experiments where X-OHT decreases, and amplifies warming in the SH in experiments where X-OHT increases (Fig 4.6j).

To understand why clouds counteract the radiative effects of water vapour between our experiments, we split the temperature change due to the total cloud feedback into the shortwave and longwave components (Fig 4.7). Figure 4.7a shows the temperature changes between experiments due to the total cloud feedback, the same as Figure 4.6j, and explained above. The temperature change due to the shortwave cloud feedback is shown in Figure 4.7b. There are clear differences

between experiments in the tropics of both hemispheres and over 30S-60S. In the NH tropics, warming due to shortwave cloud feedback is greater in experiments where X-OHT decreases (blue-hued lines); conversely, in the SH tropics, warming is greater in experiments where X-OHT increases (red-hued lines). Between 30S-60S, warming due to shortwave cloud feedback is greater in experiments with decreasing X-OHT (blue-hued lines). The temperature change attributable to the longwave cloud feedback is shown in Figure 4.7c. In the NH tropics, warming is greater in experiments where X-OHT increases (red-hued lines); whereas, in the SH tropics warming is greater in experiments where X-OHT decreases (blue-hued lines). Between 30S-60S, warming due to longwave cloud feedback is greater in experiments with increasing X-OHT (blue-hued lines). The differences in temperature change between experiments, over 30S-40S, due to shortwave and longwave cloud feedbacks cancel out (see Fig 4.7a).

The total cloud feedback is able to amplify warming in the NH in experiments where X-OHT decrease (blue-hued lines) and amplify warming in the SH in experiments where X-OHT increases (red-hued lines), because the radiative effects of low clouds on the surface climate dominate over the radiative effects of high clouds.

With increasing X-OHT (as in `X-OHT+40%` and `X-OHT+20%`), the ITCZ is located in the NH (warmer hemisphere) and further shifts northward. ITCZ shifts, alongside changes in the Hadley cells, allow the atmosphere transport the excess energy available in the warmer NH to the relatively cooler SH. In this case, the NH Hadley cell weakens and a decline in subsidence follows this weakened NH circulation. Reduced subsidence favours low-level cloudiness in regions of downward motion. Consequently, subtropical low clouds either slightly increase (as in `X-OHT+40%`) or slightly reduce (as in `X-OHT+20%`) and have a negative shortwave feedback effect in the NH (i.e., they act to cool the hemispheric surface climate). On the other hand, the SH Hadley cell strengthens with an increase in subsidence. Since strong subsidence disfavours low-level cloudiness, subtropical low clouds in the SH experience a greater reduction. They therefore have a positive shortwave feedback effect in the SH (i.e., they act to warm the hemispheric surface climate).

When X-OHT is decreased (as in `X-OHT-40%` and `X-OHT-20%`), the ITCZ shifts southward into the SH (warmer hemisphere). Changes in Hadley circulation aid the compensating transport of atmospheric energy to the relatively cooler NH. The NH Hadley cell intensifies with stronger subsidence in the NH subtropics. Therefore, subtropical low clouds in the NH are greatly reduced in `X-OHT-40%`

and X-OHT-20%, providing a dominant positive hemsipheric warming feedback. In reverse, the SH Hadley cell weakens with a decline in subsidence. Subtropical low-level cloudiness in the SH slightly decreases as a result, and dampens surface warming in the SH.

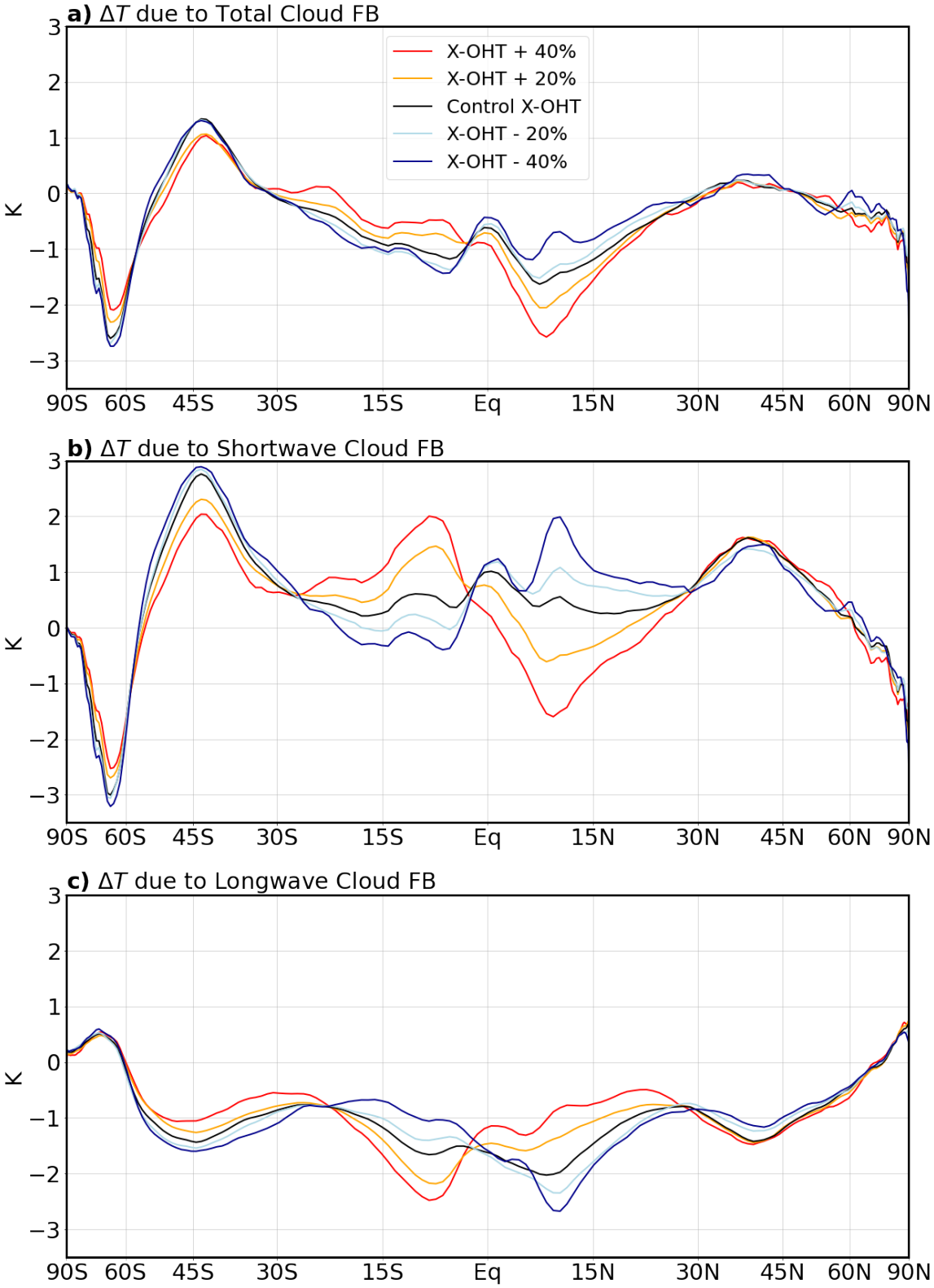

Figure 4.7.: Zonal mean temperature changes in the CESM1-SOM CO_2-doubling experiments attributable to: (a) total cloud feedback (in K); (b) shortwave cloud feedback (in K); and (c) longwave cloud feedback (in K).

.

Table 4.1.: Attribution of surface temperature change in the CESM1-SOM CO_2-doubling experiments to radiative feedbacks (Planck curvature, lapse rate, water vapour, surface albedo, and cloud), CO_2 forcing, ocean heat transport convergence, and atmospheric energy transport convergence. Shown averaged over the Northern and Southern Hemispheres. 'Spread in ΔT' column denotes the difference between the ΔT contributions in `X-OHT+40%` and `X-OHT-40%`; positive values indicate that the factor increases the spread in warming between `OHT+40%` and `OHT-40%`, while negative values indicate that the factor decreases the spread.

	CESM1-SOM Experiments					
	`X-OHT+40%`	`X-OHT+20%`	`Control X-OHT`	`X-OHT-20%`	`X-OHT-40%`	Spread in ΔT
Northern Hemisphere ΔT						
Total Feedback	2.76	2.66	2.51	2.39	2.37	0.39
Planck Curvature	-0.01	-0.01	0	0	0	-0.01
Lapse Rate FB	0.27	0.25	0.2	0.14	0.16	0.11
Water Vapor FB	2.37	2.23	2.06	1.96	1.83	0.54
Cloud FB	-0.65	-0.55	-0.46	-0.4	-0.3	-0.35
Surface Albedo FB	0.78	0.74	0.71	0.69	0.68	0.1
Forcing	1.59	1.59	1.59	1.59	1.59	0
Total Energy Transport	-0.03	-0.03	0.05	0.06	0.05	-0.08
Atmospheric Energy Transport	-0.25	-0.13	0.05	0.17	0.29	-0.54
Ocean Heat Transport	0.22	0.1	0	-0.11	-0.24	0.46
Southern Hemisphere ΔT						
Total Feedback	1.3	1.43	1.77	1.92	2.1	-0.8
Planck Curvature	0.01	0.01	0	0	0	0.01
Lapse Rate FB	-0.31	-0.29	-0.22	-0.2	-0.16	-0.15
Water Vapor FB	1.49	1.65	1.92	2.09	2.23	-0.74
Cloud FB	-0.23	-0.31	-0.36	-0.42	-0.42	0.19
Surface Albedo FB	0.35	0.37	0.43	0.45	0.46	-0.11
Forcing	1.88	1.88	1.88	1.87	1.88	0
Total Energy Transport	-0.05	-0.01	-0.07	-0.05	-0.12	0.07
Atmospheric Energy Transport	0.26	0.12	-0.05	-0.17	-0.33	0.59
Ocean Heat Transport	-0.31	-0.13	-0.02	0.12	0.21	-0.52

From area-averaging feedbacks and their sum over each hemisphere (shown in Table 4.1), we see that total water vapour (including shortwave and longwave) and total cloud (including shortwave and longwave) feedbacks contribute the most to the difference in hemispheric warming between experiments. In particular, the water vapour feedback increases differences in warming between experiments (i.e. amplifying warming in the NH and damping warming in the SH in experiments where X-OHT increases), while total cloud feedbacks oppose these (i.e. damping warming in the NH and amplifying warming in the SH in experiments where X-OHT increases).

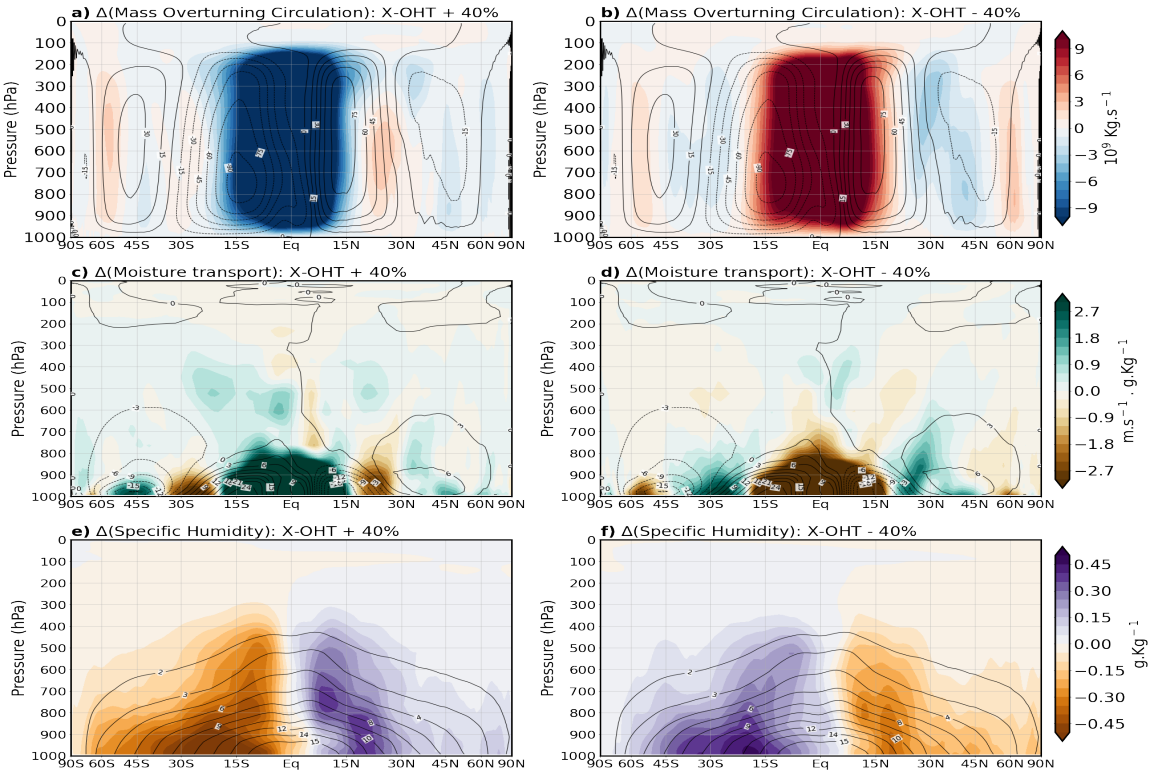

Figure 4.8.: Atmospheric circulation, moisture transport, and specific humidity responses in the CESM1-SOM CO2-doubling experiments. (a), (d), (c) change in the Eulerian mass overturning streamfunction (10^9 kg/s; colors), relative to `Control X-OHT`, shown with the preindustrial control mass overturning streamfunction (contours); (b), (e), (h) change in moisture transport (m/s . g/kg; colors), relative to `Control X-OHT`, shown with the preindustrial control moisture transport (contours); (c), (f), (i) change in the atmospheric specific humidity (g/kg; colors), relative to `Control X-OHT`, shown with the preindustrial control specific humidity (contours)

We next evaluate atmospheric dynamics to understand how changes in X-OHT impact water vapour feedbacks across our CO_2–doubling experiments, as well as their temperature change contributions. In Figure 4.8(a,b), we show the change in

the Eulerian mass overturning circulation in `X-OHT+40%` and `X-OHT-40%` relative to `Control X-OHT%`. With increased X-OHT (`X-OHT+40%`), the rising branch of the SH Hadley cell strengthens more than `Control X-OHT%` while the NH Hadley cell relatively weakens (Fig 4.8a). The atmosphere responds to X-OHT changes through changes in the Hadley cells and shifts in the ITCZ [Vellinga and Wu, 2008, Kang et al., 2008, 2009, Frierson et al., 2013, Rencurrel and Rose, 2018]. In `X-OHT+40%`, the strengthening of the SH Hadley cell is associated with a northward moisture transport (from the SH subtropics towards the ITCZ, which is located in the NH, roughly between 12 to 15N) that exceeds the transport in `Control X-OHT` (Fig 4.8c). Therefore, poleward moisture transport to the SH extratropics in `X-OHT+40%` is reduced when compared to `Control X-OHT`. Since the NH Hadley cell relatively weakens in `X-OHT+40%` (Fig. 4.8a), less moisture converges and gets uplifted in the NH tropics (Fig 4.8c). Both of these processes increase moisture availability in NH tropical areas, which can then be transported by eddies to the extra tropics. Consequently, specific humidity is reduced over the SH and increased over the NH in experiments with increasing X-OHT, relative to `Control X-OHT%` (Fig 4.8e).

On the other hand, the rising branch of the NH Hadley cell in `X-OHT-40%` strengthens more than `Control X-OHT` while the SH Hadley cell relatively weakens (Fig 4.8b). In `X-OHT-40%`, the strengthening of the NH Hadley cell is associated with a southward moisture transport (from the NH subtropics) that is stronger than the transport in `Control X-OHT%` (Fig 4.8d). Therefore, poleward moisture transport to the NH extratropics in `X-OHT-40%` is reduced when compared to `Control X-OHT%`. Since the SH Hadley cell relatively weakens in `X-OHT-40%` (Fig. 4.8b), less moisture converges and gets uplifted in the SH tropics (Fig 4.8d). Both of these processes drive increased moisture abundance in the SH tropics, which can then be transported by eddies to SH extra tropical regions. Consequently, specific humidity is reduced over the NH and increased over the SH in experiments with decreasing X-OHT, relative to `Control X-OHT%` (Fig 4.8f), and therefore controls the water vapour feedback effect on local warming.

4.4. Impacts of X-OHT Changes on the Hydrologic Cycle

To understand differences in precipitation sensitivity between CESM1-SOM experiments, we show the zonal-mean response in surface evaporation with CO_2–

doubling between the CESM1-SOM experiments in Figure 4.9(a). There are clear differences in surface evaporation between experiments at nearly all latitudes. Poleward of 10°S, evaporation changes in `X-OHT+20%` and `X-OHT+40%` are smaller than changes in `X-OHT-20%` and `X-OHT-40%`. In contrast, evaporation changes poleward of 10°N are larger in `X-OHT+20%` and `X-OHT+40%` than in `X-OHT-20%` and `X-OHT-40%`. Between 5S to 10S, increase in evaporation is greater in `X-OHT+20%` and `X-OHT+40%` than the increase in `X-OHT-20%` and `X-OHT-40%`. On the other hand, between 5N to 10N, increase in evaporation is greater in `X-OHT-20%` and `X-OHT-40%` than the increase in `X-OHT+20%` and `X-OHT+40%`.

More ocean heat converges in the NH when X-OHT is increased (`X-OHT+20%` and `X-OHT+40%`), with greater poleward export from the NH tropics to NH extratropical areas (Fig. 4.4a). When X-OHT is decreased (`X-OHT-20%` and `X-OHT-40%`), more ocean heat converges in the SH, with greater poleward export from the SH tropics to SH extratropical areas (Fig. 4.4a). Therefore, differences in evaporation between 5°to 10°and also poleward of 10°in both hemispheres are consistent with Sutton and Mathieu [2002], who showed that changes in ocean heat transport convergence are mainly balanced by latent heat flux changes, in the form of increased evaporation.

Equatorward of 5°S, the increase in evaporation is greater in experiments with decreasing X-OHT (red-hued lines) than in experiments with increasing X-OHT (blue-hued lines). Whereas evaporation changes are less clear equatorward of 5°N, with greater evaporation increase in `X-OHT-20%` and `X-OHT+20%` than in `X-OHT-40%` and `X-OHT+40%`. Equatorward of 5°S, where the pattern of differences are clearer compared to the NH deep tropics, experiments with decreasing X-OHT (blue-hued lines) show greater evaporation changes because surface temperature increase over a weak wind zone (in this case, the SH region of Hadley cell weakening relative to the NH cell as in Fig. 4.8b), drives an increase in the release of evaporation.

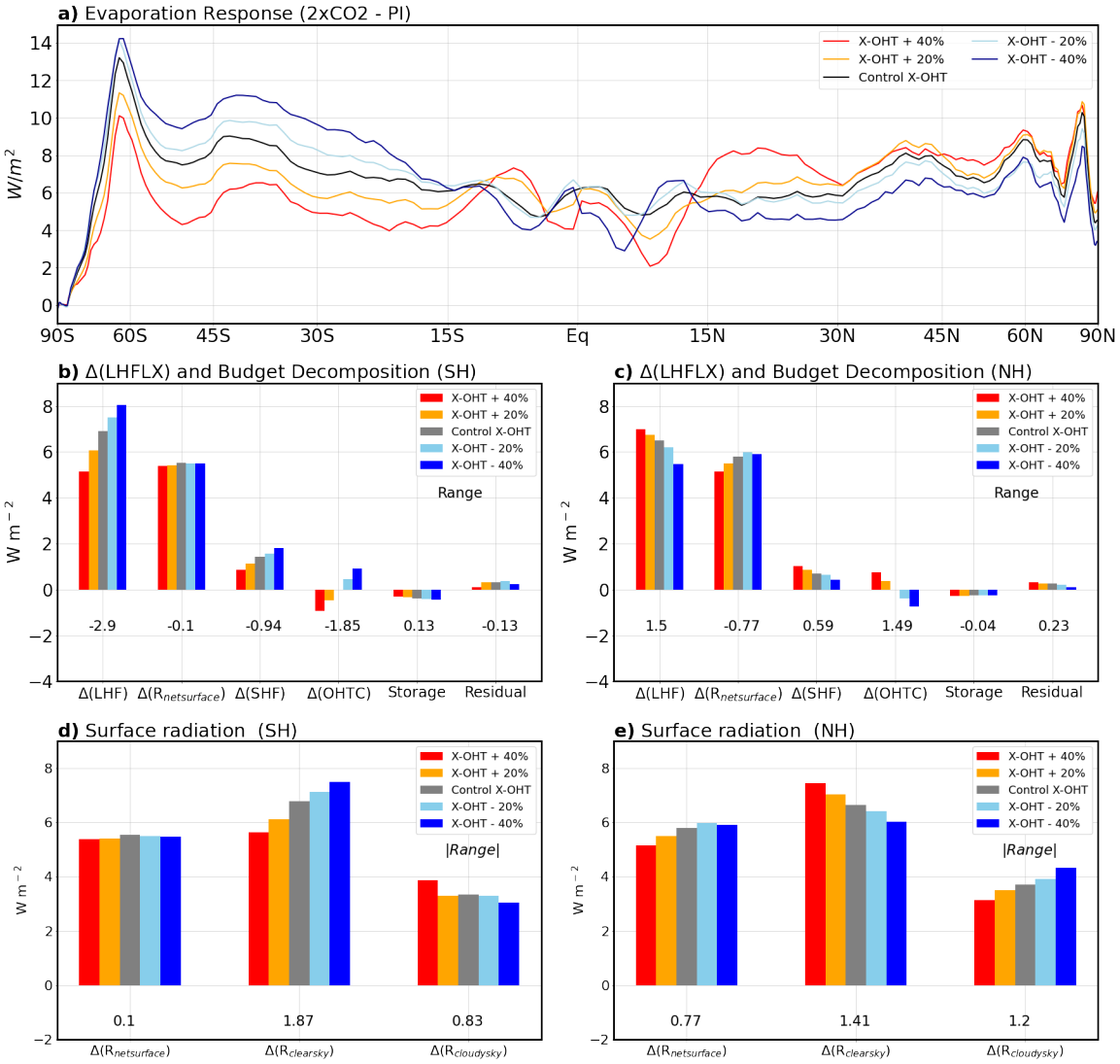

Figure 4.9.: a) Zonal mean change in surface evaporation (LHF; in W m^{-2}) in the CESM1-SOM CO_2-doubling experiments; budget contributions from changes in ocean heat transport convergence (OHTC; in W m^{-2}), net surface radiation ($R_{netsurface}$; in W m^{-2}), sensible heat flux (SHF; in W m^{-2}), ocean storage (in W m^{-2}), and residual (in W m^{-2}) of the decomposition between b) 90S to the equator and c) the equator to 90N; and all-sky (net), clear-sky, and cloudy sky surface radiation between d) 90S to the equator and e) the equator to 90N.

In Figures 4.9(b,c), we decompose the hemispheric response in surface evaporation (LHF), following Equation (4.5), in order to understand contributions from changes in ocean heat transport convergence ($-\nabla \cdot OHT$), net surface radiation ($\mathrm{R}_{netsurface}$), sensible heat flux (SHF), and the rate of heat storage in the slab ocean mixed layer (dE_{ocn}/dt).

$$\Delta(LHF) = \Delta(R_{netsurface}) - \Delta(SHF) + \Delta(-\nabla \cdot OHT) - \Delta(\frac{dE_{ocn}}{dt}) \qquad (4.5)$$

For each of the terms in the evaporation budget equation, we calculate the range between experiments as the difference between `X-OHT+40%` and `X-OHT-40%`. The range is shown below each set of bars of individual terms in Figure 4.9(b,c). We find that range in OHTC changes explain 63% of the range in LHF changes between experiments in the SH (Fig. 4.9b). The next largest contributing term is SHF changes with 32%. In the SH, $\mathrm{R}_{netsurface}$ changes and storage vary little between experiments, so do not contribute to differences in surface evaporation. In the NH, ocean heat transport convergence changes are also the most important contributor to differences in Δ(LHF) between experiments (Fig. C4.9c), accounting for 98% of the range. The next most important terms are SHF changes (40%), while $\mathrm{R}_{netsurface}$ changes oppose differences in LHF changes (-51%).

While differences in ocean heat transport convergence between experiments clearly drive differences in evaporation in both hemispheres, some of the variance in surface evaporation is due to variance in the radiative effects of clouds, particularly in the NH. In Figures 4.9(b,c), we see that net surface radiation variance between experiments contribute to the variance in evaporation more in the NH than the SH: the magnitude of variance in the SH is 0.1 W m^{-2} and 0.77 W m^{-2} in the NH. We explore this associated impact in Figures 4.9(d,e), where we show how clouds impact the variance in evaporation between experiments by affecting net surface radiation. The first set of bars in Figures 4.9(d,e) display the change in net (all-sky) surface radiation, $\mathrm{R}_{netsurface}$, between experiments (reproduced as in Figures 4.9b,c). $\mathrm{R}_{netsurface}$ is the weighted sum of the clear-sky (no clouds) surface radiation, $\mathrm{R}_{clearsky}$, and cloudy-sky (clouds present) surface radiation, $\mathrm{R}_{cloudysky}$. The magnitude of the range between experiments (`X-OHT+40%` minus `X-OHT-40%`) is given below each set of bars. We find that in the SH, the magnitude of the variance in net surface radiation between experiments is larger under clear-sky conditions than in the presence of clouds (Fig. 4.9d), i.e., clouds reduce this by 1.04 W m^{-2}. In the NH, the effects of clouds on surface radiation also decrease the magnitude of variance between experiments, from 1.41 W m^{-2} to 1.2 W m^{-2} (Fig.

4.9e). This 0.2 W m^{-2} change in the NH is smaller than what the SH experiences due to clouds.

Our results show that differences in X-OHT between experiments, which affect hemispheric ocean heat transport convergence, determine the hemispheric hydrologic cycle response through the impact of ocean heating on surface evaporation.

5: Mechanisms Underlying AMOC Impact on Climate and the Hydrologic Cycle in CMIP6

In our CESM1-SOM experiments, changes in ocean heat transport convergence determine the climate and precipitation response through the impact of ocean heating on water vapour and evaporation. We have already shown that there is a similar relationship between AMOC changes (which further drive X-OHT changes in a fully-coupled climate) and the hemispheric climate and precipitation response in CMIP6 (recall Fig 3.2). CMIP6 ESMs with stronger AMOC decline tend to display more comparable warming between the NH and SH. On the other, in ESMs with a weaker AMOC decline, the NH tends to warm more than the SH. Furthermore, ESMs with stronger AMOC decline generally exhibit greater precipitation increase in the SH than in the NH, while ESMs with weaker AMOC decline show greater precipitation increase in the NH than in the SH. We next assess if the impact of AMOC changes on the hemispheric climate and hydrologic response depends on similar mechanisms as those found in our CESM-SOM1 experiments.

5.1. Spatial Pattern of AMOC Impact on Climate and the Hydrologic Cycle Response

To understand how intermodel variance in AMOC decline may co-vary with intermodel variance in the surface climate, we regress surface warming and precipitation changes on AMOC decline and evaluate the climate and hydrologic cycle response when AMOC decline is 2 standard deviations below the multi-model mean (-14 Sv, which is 2 standard deviations below the multimodel mean of -10.5 Sv). The SH (excluding South America) warms more than average when there is a strong decline in the AMOC (Fig. 5.1a) and the NH warms less than average. This result

supports an earlier finding of Lin et al. [2019]: that the intermodel range in the AMOC response co-varies inversely (directly) with the range of NH (SH) warming in CMIP5 class ESMs.

We also find a similar impact on the precipitation response. For a 14 Sv decline in the AMOC, tropical precipitation increases south of the equator, relative to the mean precipitation response, and decreases north of the equator. This suggests that the ITCZ moves southward when AMOC strongly declines, consistent with Frierson et al. [2013]. Precipitation in the SH mid-latitude storm track region also intensifies more than average (Fig 5.1c). Generally, there is an increase in precipitation in most parts of the SH relative to the mean precipitation response. On the other hand, we note a decrease in precipitation over large areas in the NH, relative to the mean precipitation response. Spatial significance at 95% confidence level is generally noted in higher latitudes of the North Atlantic basin, the tropics, and Southern high latitudes.

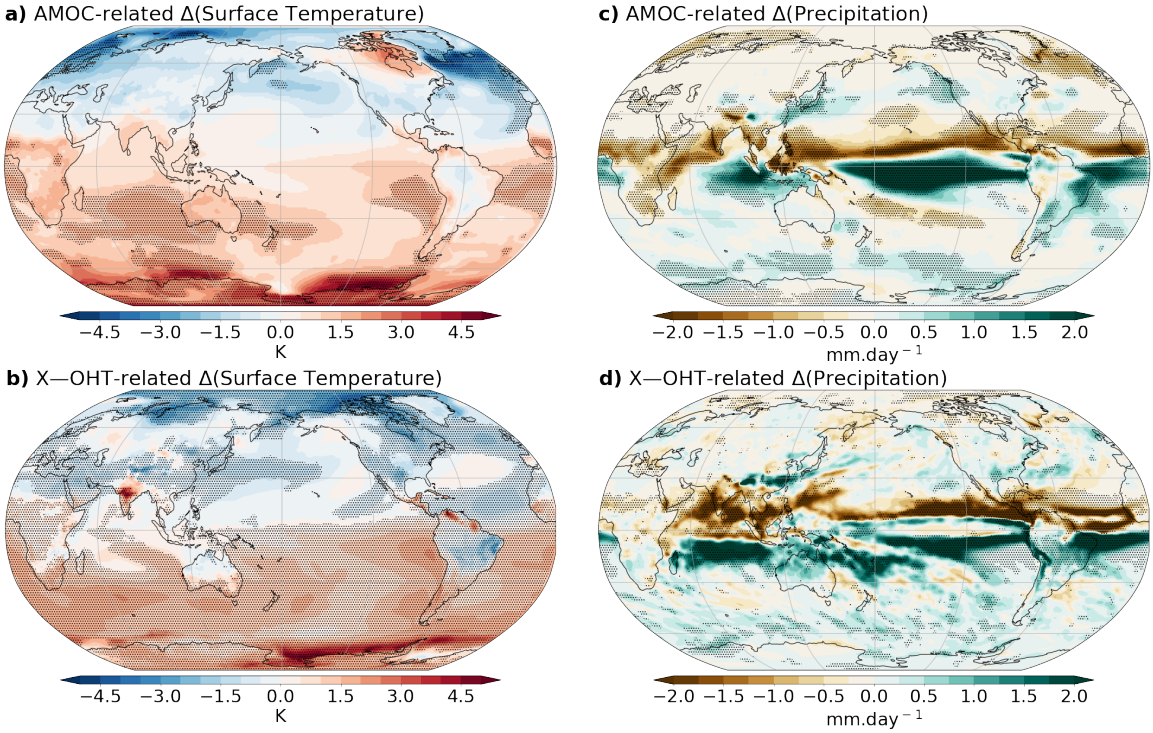

Figure 5.1.: Linear regression of a,b) change in surface temperature (in K); and c,d) precipitation change (in mm/day) on a 14Sv AMOC decline in CMIP6 and a 0.48 PW decline in X-OHT in the CESM1-SOM CO_2-doubling experiments respectively. Stippling denotes the significance at 95% confidence level

As in CMIP6, we regress temperature and hydrologic cycle changes on assessed AMOC changes in our CESM1-SOM experiments. In CMIP6, a two standard

deviation AMOC decline (approximately 14 Sv) corresponds to a 0.48 PW X-OHT decline. Therefore, we regress surface warming and precipitation changes on X-OHT decline in our CESM1-SOM experiments and evaluate this when X-OHT decline is 0.48 PW (Fig.5.1b,d).

Figure 5.1b shows that strong X-OHT decline causes much of the SH and monsoon regions in the NH deep tropics to experience more surface warming, relative to when X-OHT is unchanged, and causes much of the NH (especially poleward of 15N) to experience relatively less surface warming. The increased relative warming (up to 4.5K) is greatest over the Indian monsoon region, Southern ocean, Antarctic peninsula, and the regional seas around Antarctica (Weddell, Amundsen, Bellingshausen, and Ross). Meanwhile, the Labrador and Nordic seas where the AMOC typically sinks see the weakest level of warming with strong decline of X-OHT. In addition to surface warming, strong X-OHT decline also plays a role in how precipitation responds regionally (Fig 5.1d), relative to when X-OHT is unchanged. Overall, we note that precipitation increases more over the SH than the NH when X-OHT increases, relative to when X-OHT is unchanged. Surprisingly, subtropical drying appears to be enhanced over the ocean in the SH, and suppressed over NH land areas. However, this is not statistically significant. Over the deep tropics, particularly across ocean basins, we also see precipitation increases exceeding 2 mm/day in magnitude, and indication of a southward ITCZ shift. X-OHT—associated change in precipitation is statistically significant in the tropics and parts of high latitudes in both hemispheres. Therefore, the large-scale spatial pattern of the AMOC-related and X-OHT related hemispheric CO_2–forcing response are comparable between CMIP6 models and our CESM1-SOM experiments (compare Fig. 5.1a,c to 5.1b,d). However, we note that the magnitude of response over the North Atlantic is smaller in the CESM1-SOM regression and there is statistical significance over more areas in the CESM1-SOM regression (Figure 5.1b) than in the CMIP6 intermodel regression (Figure 5.1d). These differences likely arise from regional differences in how X-OHT changes: in the CMIP6 regression, the AMOC index is defined in the North Atlantic basin and the decline in X-OHT is limited to this basin. In contrast, in the CESM1-SOM experiments, X-OHT decline is the decline in the net cross-equatorial OHT, achieved by applying zonally-symmetric OHFC anomalies. Therefore, X-OHT decline is not limited to the Atlantic basin in the CESM1-SOM experiments.

5.2. Mechanisms Governing AMOC-related Impact in CMIP6

We have shown that the climatic impacts of AMOC decline in CMIP6 and X-OHT decline in CESM1-SOM are comparable. Analysis of the CMIP6 multi-model ensemble suggests that the mechanisms driving these relationships in CMIP6 and CESM1-SOM are similar. As in our CESM1-SOM experiments that show causality, we find that ocean heat convergence by the AMOC in CMIP6 also co-varies with differences in the regional response to CO_2–forcing. In ESMs analyzed, AMOC weakening is strongly related to X-OHT decline, which decreases upper ocean heat content in the SH and increases it in the NH. Differences in upper ocean heat content between hemispheres help drive differences in atmospheric water vapour content and evaporation between hemispheres. This, in turn, helps explain the hemispheric difference in surface temperature and hydrologic cycle response, as in our CESM1-SOM experiments, which were causative.

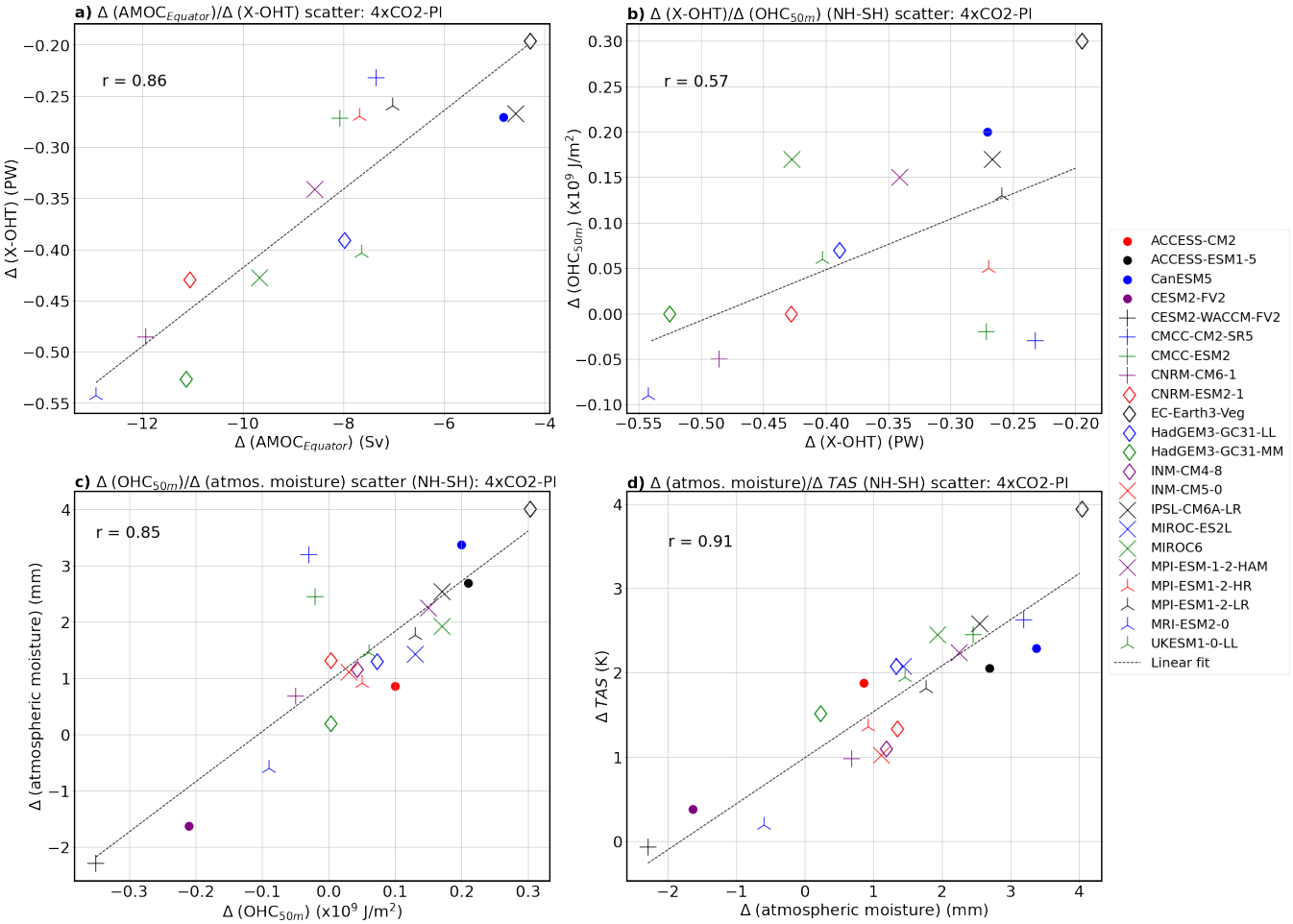

Figure 5.2.: Mechanism for the relationship between the hemispheric difference in climate sensitivity (Northern hemisphere minus Southern hemisphere; in K) and change in the maximum strength of the AMOC (Sv). Linear regression between a) AMOC change (evaluated at the equator) and change in northward, cross-equatorial ocean heat transport in the Atlantic basin (Atlantic OHT; in PW); b) change in northward, cross-equatorial OHT and hemispheric difference in upper-ocean heat content change (OHC; in $\times 10^9$ J/m^2); c) hemispheric differences in upper-ocean heat content change and atmospheric moisture content change (in mm); and d) hemispheric differences in atmospheric moisture content change and climate sensitivity (TAS; in K). Calculated over years 120-150 of `abrupt-4xCO2`, relative to `piControl`. Correlations are statistically significant at $p < 0.05$.

The upper branch of the AMOC moves ocean heat northward and across the equator. Therefore, AMOC weakening, evaluated at the equator, drives a reduction in Atlantic X-OHT. This is evident in models of interest that provided the CMIP6 variable, *hfbasin* (Fig. 5.2a). Changes in the AMOC also control hemispheric differences in upper ocean heat content through changes in the amount of energy it moves across the equator, into the NH. This is also evident in CMIP6 (Fig. 5.2b), where we find models with a stronger reduction in X-OHT have a smaller upper ocean heat content in the NH, and vice-versa in models with weaker X-OHT reduction. We evaluate ocean heat content over the first 50m of the ocean and not over the mixed-layer depth to allow for model inter-comparison and to account for differing lateral resolution and mixed-layer biases [Constantinou and Hogg, 2021]. We find that changes in atmospheric water vapour content are largely affected by the magnitude of surface heating available and supplied by the ocean. CMIP6 models that have a larger increase in NH upper ocean heat content relative to the SH also exhibit a greater increase in atmospheric water vapour content in the NH (Fig. 5.2c). On the other hand, ESMs with a larger increase in upper ocean heat content in the SH exhibit a greater increase in atmospheric water vapour content in the SH also (Fig. 5.2c). Finally, the hemisphere with a larger increase in atmospheric water vapor content has additional moisture that increases the CO_2 greenhouse effect. The atmospheric water vapour feedback in that hemisphere then amplifies the hemispheric climate response to a quadrupling of atmospheric CO_2 more than the hemisphere with a smaller increase in atmospheric water vapour. Therefore, there is a strong relationship between hemispheric differences in surface warming and water vapour content in CMIP6 (Fig. 5.2d). This is consistent to our findings from CESM1-SOM where prescribed X-OHT affects radiative feedback variables, especially water vapour which contributes the most to differences in surface warming between experiments at nearly all latitudes (see Figures 4.6a,b and 4.6c,j).

In terms of the hydrologic cycle response, we also find that the mechanism operating in our CESM1-SOM results are applicable in CMIP6. Recall that differences in ocean heat flux convergence explain over half of the differences in evaporation changes between hemispheres, and controls the hydrologic cycle response in our CESM1-SOM experiments (Fig 4.9b). AMOC decline in CMIP6 impacts changes in X-OHT and hemispheric differences in upper ocean heat content in the same manner as explained above (Fig. 5.3a,b). CMIP6 models with a larger increase in NH upper ocean heat content relative to the SH exhibit a greater evaporation increase in the NH (Fig. 5.3c), and vice versa when increase

in upper ocean heat content in the NH is smaller than in the SH. Therefore, there is a strong relationship between hemispheric differences in evaporation changes and the hydrologic cycle response, especially precipitation sensitivity (Fig. 5.3d) which greatly varies between CMIP6 ESMs and is often challenging to physically constrain.

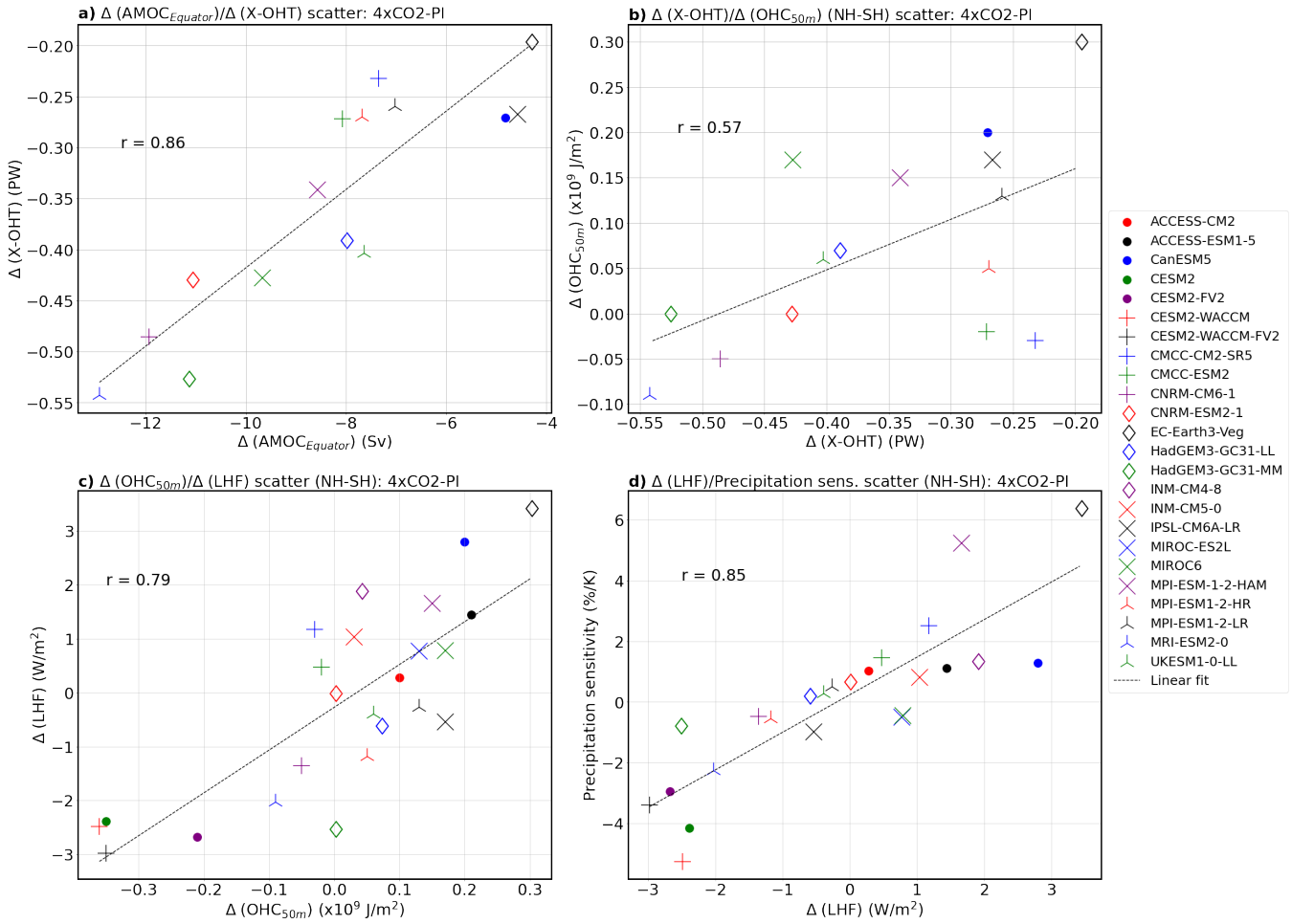

Figure 5.3.: Mechanism for the relationship between the hemispheric difference in precipitation sensitivity (Northern hemisphere minus Southern hemisphere; in %/K) and change in the maximum strength of the AMOC (Sv). Linear regression between a) AMOC change (evaluated at the equator) and change in northward, cross-equatorial ocean heat transport (OHT; in PW) b) change in northward, cross-equatorial OHT and hemispheric difference in upper-ocean heat content change (OHC; in x10^9 J/m^2) c) hemispheric differences in upper-ocean heat content change and evaporation (LHF) change (in mm) d) hemispheric differences in LHF change and hydrologic cycle sensitivity (in %/K). Calculated over years 120-150 of `abrupt-4xCO2`, relative to `piControl`. Correlations are statistically significant at $p < 0.05$.

6: Conclusion

Earth system models exhibit weakening of the AMOC and diminishing northward cross-equatorial ocean heat transport (X-OHT) in response to an increase in atmospheric greenhouse gas concentrations. A number of studies that isolate the climate impacts of AMOC weakening in response to greenhouse gas forcing commonly do so through freshwater perturbations in the North Atlantic [see Chapter 1; Vellinga and Wood, 2008, Zickfeld et al., 2008, Kuhlbrodt et al., 2009, Liu et al., 2020]. This freshwater perturbation method to impose AMOC changes may unintentionally set up circulation responses in other ocean basins. Therefore, the climate response in these studies also includes competing ocean circulation perturbations and associated feedbacks, not only the impacts of AMOC weakening.

Given that a major imprint of AMOC weakening is declining X-OHT, we focus on the independent impact of X-OHT on the regional CO_2–doubling response in a set of idealized sensitivity experiments (see Chapter 2 for experimental setup). We directly perturb X-OHT over a wide range in CESM1-SOM and assess impacts on the regional climate and hydrologic cycle response to abrupt CO_2–doubling. Prescribed ocean heat transport anomaly is well compensated by atmospheric energy transport response across our experiments, consistent with previous studies [Bjerknes, 1964, Shaffrey and Sutton, 2006, Farneti and Vallis, 2013, Yang et al., 2015]. The atmosphere is able to compensate through changes in the Hadley circulation and displacements of the Intertropical Convergence Zone (ITCZ). We find that regional climate and precipitation responses are sensitive to changes in X-OHT, in and outside the deep tropics. CO_2–doubling experiments with increases in X-OHT (`X-OHT+20%` and `X-OHT+40%`) generally exhibit more surface warming and a higher precipitation sensitivity in the NH than in the SH. In contrast, CO_2–doubling experiments with reductions in X-OHT (`X-OHT-20%` and `X-OHT-40%`) generally display less warming and lower precipitation sensitivity in the NH than in the SH. We show that differences in the strength of the zonal-mean total water vapour feedbacks largely explain the difference in the zonal-mean warming pattern over most latitudes across our experiments. The total cloud feedback opposes the

total water vapour feedback and also contributes to the difference in zonal-mean warming over the tropics and SH mid-latitudes (45°S to 65°S).

From a zonal-mean or regional perspective, surface warming has been shown to be driven by radiative forcing, the strength of surface and atmospheric radiative feedbacks, and the net effects of deepwater exchange and heat transport by ocean circulation [Bonan et al., 2018]. Interestingly, our results reveal that changes in ocean heat flux convergence (OHFC) directly affects water vapour in the tropics and cloud feedbacks, both in the tropics and between 45-60S, which then determine difference in surface warming across our experiments. Furthermore, a hemispheric evaporation budget analyses reveal that differences in OHFC contribute the most to the difference in evaporation, which is an important factor controlling how the hydrologic cycle responds to warming [Sutton and Mathieu, 2002, Held, 2001, Siler et al., 2019, Liu et al., 2020]. Our results suggests that ocean dynamics control the regional climate and hydrologic response to an increase in CO_2, even outside the deep tropics. In particular, changes in X-OHT and therefore OHFC, determine the response by affecting radiative feedbacks (particularly water vapour and cloud) and supplying the required heat for enhanced surface evaporation.

We take our energetic approach further and evaluate the applicability of our idealized CESM1-SOM results in CMIP6 models. As we show (in Fig.3.1c), decline of the AMOC in response to abrupt CO_2–quadrupling is evident among CMIP6 models, albeit with a large spread. The intermodel range in AMOC decline is closely related to the intermodel range in hemispheric asymmetries in surface warming and precipitation sensitivity. Models with stronger AMOC decline display less warming and a smaller precipitation sensitivity in the NH relative to the SH, while models with weaker AMOC decline display more warming and a higher precipitation sensitivity in the NH relative to the SH. We propose a mechanism related to water vapour and evaporation, identical to what we find governing our CESM1-SOM results, to explain these relationships in CMIP6: a strong AMOC decline (of order 14 SV which exceeds two standard deviations of the mean decline) causes a reduction in X-OHT, which then leads to a smaller upper ocean heat content in the NH relative to the SH. Consequently, atmospheric water vapour is reduced and surface evaporation is suppressed in the NH, accounting for less warming and smaller precipitation sensitivity respectively in the NH compared to the SH.

We must acknowledge that there are important caveats to consider. First, recent studies show that southward cross-equatorial ocean heat transport is non-

negligible in the Indian ocean [Trenberth and Fasullo, 2017, Forget and Ferreira, 2019]. This cross-equatorial ocean heat transport in associated with the presence of land to the north of the Indian basin [Forget and Ferreira, 2019] and is possibly facilitated by shallow meridional overturning circulations. However, the northward cross-equatorial ocean heat transport in the Atlantic due to the AMOC is larger and dominates net X-OHT. We have not considered the impact of the Indian cross-equatorial ocean heat transport on the climate response to CO_2 forcing, which may also be an important part of the regional climate response. Secondly, the use of CESM1-SOM alone to establish causality could produce results and show mechanisms that are specific to the model framework. However, we note that the CESM is state-of-the art and mostly produces a realistic representation of Earth's mean climate and the hydrologic cycle.

In summary, our results highlight the importance of ocean dynamics in determining asymmetries in the hemispheric climate response to CO_2 forcing, particularly how much regional precipitation changes with warming. It is necessary to investigate and identify the possible role of ocean dynamics in setting other hemispheric asymmetries and symmetries in the present-day climate (e.g. Earth's planetary albedo), as well as in a warmer world.

Bibliography

Kevin E Trenberth and Julie M Caron. Estimates of meridional atmosphere and ocean heat transports. *Journal of Climate*, 14(16):3433–3443, 2001.

Isaac M Held. The partitioning of the poleward energy transport between the tropical ocean and atmosphere. *Journal of the Atmospheric Sciences*, 58(8): 943–948, 2001.

Carl Wunsch. The total meridional heat flux and its oceanic and atmospheric partition. *Journal of climate*, 18(21):4374–4380, 2005.

Michael Winton. On the climatic impact of ocean circulation. *Journal of climate*, 16(17):2875–2889, 2003.

Celine Herweijer, Richard Seager, Michael Winton, and AMY Clement. Why ocean heat transport warms the global mean climate. *Tellus A: Dynamic Meteorology and Oceanography*, 57(4):662–675, 2005.

Marcelo Barreiro, Annalisa Cherchi, and Simona Masina. Climate sensitivity to changes in ocean heat transport. *Journal of climate*, 24(19):5015–5030, 2011.

M Cameron Rencurrel and Brian EJ Rose. Exploring the climatic response to wide variations in ocean heat transport on an aquaplanet. *Journal of Climate*, 31(16):6299–6318, 2018.

Richard Seager, David S Battisti, J Yin, Neil Gordon, Naomi Naik, Amy C Clement, and Mark A Cane. Is the gulf stream responsible for europe's mild winters? *Quarterly Journal of the Royal Meteorological Society: A journal of the atmospheric sciences, applied meteorology and physical oceanography*, 128 (586):2563–2586, 2002.

Peter Rhines, Sirpa Häkkinen, and Simon A Josey. Is oceanic heat transport significant in the climate system? In *Arctic–subarctic ocean fluxes*, pages 87–109. Springer, 2008.

Ayako Yamamoto, Jaime B Palter, M Susan Lozier, Michel S Bourqui, and Susan J Leadbetter. Ocean versus atmosphere control on western European wintertime temperature variability. *Climate dynamics*, 45(11):3593–3607, 2015.

TH Vonder Haar and Abraham H Oort. New estimate of annual poleward energy transport by northern hemisphere oceans. *Journal of Physical Oceanography*, 3 (2):169–172, 1973.

Abraham H Oort and Thomas H Vonder Haar. On the observed annual cycle in the ocean-atmosphere heat balance over the northern hemisphere. *Journal of Physical Oceanography*, 6(6):781–800, 1976.

Kevin E Trenberth. Mean annual poleward energy transports by the oceans in the southern hemisphere. *Dynamics of Atmospheres and Oceans*, 4(1):57–64, 1979.

Kooiti Masuda. Meridional heat transport by the atmosphere and the ocean: analysis of FGGE data. *Tellus A*, 40(4):285–302, 1988.

BC Carissimo, AH Oort, and TH Vonder Haar. Estimating the meridional energy transports in the atmosphere and ocean. *Journal of Physical Oceanography*, 15 (1):82–91, 1985.

Rick Lumpkin and Kevin Speer. Global ocean meridional overturning. *Journal of Physical Oceanography*, 37(10):2550–2562, 2007.

Kevin E Trenberth and John T Fasullo. Atlantic meridional heat transports computed from balancing Earth's energy locally. *Geophysical Research Letters*, 44 (4):1919–1927, 2017.

Gaël Forget and David Ferreira. Global ocean heat transport dominated by heat export from the tropical Pacific. *Nature Geoscience*, 12(5):351–354, 2019.

John Marshall and R Alan Plumb. *Atmosphere, ocean and climate dynamics: an introductory text*. Elsevier, 2007.

Martha W Buckley and John Marshall. Observations, inferences, and mechanisms of the Atlantic Meridional Overturning Circulation: A review. *Reviews of Geophysics*, 54(1):5–63, 2016.

Barry A Klinger and Thomas WN Haine. *Ocean circulation in three dimensions*. Cambridge University Press Cambridge, UK, 2019.

Jeff R Knight, Robert J Allan, Chris K Folland, Michael Vellinga, and Michael E Mann. A signature of persistent natural thermohaline circulation cycles in observed climate. *Geophysical Research Letters*, 32(20), 2005.

Michael Vellinga and Richard A Wood. Global climatic impacts of a collapse of the Atlantic thermohaline circulation. *Climatic change*, 54(3):251–267, 2002.

Daniela Jacob, Holger Goettel, Johann Jungclaus, Michael Muskulus, Ralf Podzun, and Jochem Marotzke. Slowdown of the thermohaline circulation causes enhanced maritime climate influence and snow cover over Europe. *Geophysical research letters*, 32(21), 2005.

LC Jackson, R Kahana, T Graham, MA Ringer, T Woollings, JV Mecking, and RA Wood. Global and European climate impacts of a slowdown of the AMOC in a high resolution GCM. *Climate dynamics*, 45(11):3299–3316, 2015.

Salil Mahajan, Rong Zhang, and Thomas L Delworth. Impact of the Atlantic meridional overturning circulation (AMOC) on Arctic surface air temperature and sea ice variability. *Journal of Climate*, 24(24):6573–6581, 2011.

Sarah M Kang, Isaac M Held, Dargan MW Frierson, and Ming Zhao. The response of the ITCZ to extratropical thermal forcing: Idealized slab-ocean experiments with a GCM. *Journal of Climate*, 21(14):3521–3532, 2008.

Sarah M Kang, Dargan MW Frierson, and Isaac M Held. The tropical response to extratropical thermal forcing in an idealized GCM: The importance of radiative feedbacks and convective parameterization. *Journal of the atmospheric sciences*, 66(9):2812–2827, 2009.

Dargan MW Frierson, Yen-Ting Hwang, Neven S Fučkar, Richard Seager, Sarah M Kang, Aaron Donohoe, Elizabeth A Maroon, Xiaojuan Liu, and David S Battisti. Contribution of ocean overturning circulation to tropical rainfall peak in the Northern Hemisphere. *Nature Geoscience*, 6(11):940–944, 2013.

J Marshall, A Donohoe, David Ferreira, and D McGee. The ocean's role in setting the mean position of the Inter-Tropical Convergence Zone. *Climate Dynamics*, 42(7):1967–1979, 2014.

Eduardo Moreno-Chamarro, J Marshall, and TL Delworth. Linking ITCZ migrations to the AMOC and North Atlantic/Pacific SST decadal variability. *Journal of Climate*, 33(3):893–905, 2020.

James Croll. XII. On ocean-currents, part i: ocean-currents in relation to the distribution of heat over the globe. *Philosophical Magazine and Journal of Science*, 39(259):81–106, 1870.

Georg Feulner, Stefan Rahmstorf, Anders Levermann, and Silvia Volkwardt. On the origin of the surface air temperature difference between the hemispheres in Earth's present-day climate. *Journal of Climate*, 26(18):7136–7150, 2013.

Sarah M Kang, Richard Seager, Dargan MW Frierson, and Xiaojuan Liu. Croll revisited: Why is the northern hemisphere warmer than the southern hemisphere? *Climate Dynamics*, 44(5):1457–1472, 2015.

Wallace S Broecker. Thermohaline circulation, the Achilles heel of our climate system: will man-made CO2 upset the current balance? *Science*, 278(5343): 1582–1588, 1997.

Meric Srokosz, Molly Baringer, Harry Bryden, Stuart Cunningham, T Delworth, S Lozier, Jochem Marotzke, and Rowan Sutton. Past, present, and future changes in the Atlantic meridional overturning circulation. *Bulletin of the American Meteorological Society*, 93(11):1663–1676, 2012.

Wilbert Weijer, Wei Cheng, Oluwayemi A Garuba, Aixue Hu, and BT Nadiga. CMIP6 models predict significant 21st century decline of the Atlantic Meridional Overturning Circulation. *Geophysical Research Letters*, 47(12):e2019GL086075, 2020.

Michael Vellinga and Richard A Wood. Impacts of thermohaline circulation shutdown in the twenty-first century. *Climatic Change*, 91(1):43–63, 2008.

Kirsten Zickfeld, Michael Eby, and Andrew J Weaver. Carbon-cycle feedbacks of changes in the Atlantic meridional overturning circulation under future atmospheric co2. *Global Biogeochemical Cycles*, 22(3), 2008.

Till Kuhlbrodt, Stefan Rahmstorf, Kirsten Zickfeld, Frode Bendiksen Vikebø, Svein Sundby, Matthias Hofmann, Peter Michael Link, Alberte Bondeau, Wolfgang Cramer, and Carlo Jaeger. An integrated assessment of changes in the thermohaline circulation. *Climatic Change*, 96(4):489–537, 2009.

Yuan-Jen Lin, Yen-Ting Hwang, Paulo Ceppi, and Jonathan M Gregory. Uncertainty in the evolution of climate feedback traced to the strength of the Atlantic meridional overturning circulation. *Geophysical Research Letters*, 46(21):12331–12339, 2019.

Wei Liu, Alexey V Fedorov, Shang-Ping Xie, and Shineng Hu. Climate impacts of a weakened Atlantic Meridional Overturning Circulation in a warming climate. *Science advances*, 6(26):eaaz4876, 2020.

Maria AA Rugenstein, Michael Winton, Ronald J Stouffer, Stephen M Griffies, and Robert Hallberg. Northern high-latitude heat budget decomposition and transient warming. *Journal of climate*, 26(2):609–621, 2013.

Sybren Drijfhout, Geert Jan Van Oldenborgh, and Andrea Cimatoribus. Is a decline of AMOC causing the warming hole above the North Atlantic in observed and modeled warming patterns? *Journal of Climate*, 25(24):8373–8379, 2012.

Katinka Bellomo, Michela Angeloni, Susanna Corti, and Jost von Hardenberg. Future climate change shaped by inter-model differences in Atlantic meridional overturning circulation response. *Nature Communications*, 12(1):1–10, 2021.

Tim Woollings, Jonathan M Gregory, Joaquim G Pinto, Mark Reyers, and David J Brayshaw. Response of the North Atlantic storm track to climate change shaped by ocean–atmosphere coupling. *Nature Geoscience*, 5(5):313–317, 2012.

Jeremy Leggett, William J Pepper, Rob J Swart, J Edmonds, LG Meira Filho, Irving Mintzer, and MX Wang. Emissions scenarios for the IPCC: an update. *Climate change*, 1040:75–95, 1992.

William Pepper. Emission scenarios for the IPCC, an update, assumptions, methodology, and results. *Prepared for the Intergovernmental Panel on Climate Change, Working Group 1*, 1992.

Nebojsa Nakicenovic and Rob Swart. Emissions scenarios-special report of the Intergovernmental Panel on Climate Change. *Prepared for the Intergovernmental Panel on Climate Change, Working Group III*, 2000.

Shineng Hu and Alexey V Fedorov. Indian ocean warming can strengthen the atlantic meridional overturning circulation. *Nature climate change*, 9(10):747–751, 2019.

Shineng Hu and Alexey V Fedorov. Indian ocean warming as a driver of the north atlantic warming hole. *Nature communications*, 11(1):1–11, 2020.

K McMonigal, Kathryn L Gunn, Lisa M Beal, Shane Elipot, and Josh K Willis. Reduction in meridional heat export contributes to recent indian ocean warming. *Journal of Physical Oceanography*, 52(3):329–345, 2022.

Young-Min Yang, Jae-Heung Park, Soon-Il An, Sang-Wook Yeh, Zhiwei Zhu, Fei Liu, Juan Li, June-Yi Lee, and Bin Wang. Increased indian ocean-north atlantic ocean warming chain under greenhouse warming. *Nature communications*, 13 (1):1–9, 2022.

Veronika Eyring, Sandrine Bony, Gerald A Meehl, Catherine A Senior, Bjorn Stevens, Ronald J Stouffer, and Karl E Taylor. Overview of the Coupled Model Intercomparison Project Phase 6 (CMIP6) experimental design and organization. *Geoscientific Model Development*, 9(5):1937–1958, 2016.

James W Hurrell, Marika M Holland, Peter R Gent, Steven Ghan, Jennifer E Kay, Paul J Kushner, J-F Lamarque, William G Large, D Lawrence, Keith Lindsay, et al. The community earth system model: a framework for collaborative research. *Bulletin of the American Meteorological Society*, 94(9):1339–1360, 2013.

C.M. Bitz, K.M. Shell, P.R. Gent, D.A. Bailey, G. Danabasoglu, K.C. Armour, M.M. Holland, and J.T. Kiehl. Climate sensitivity in the Community Climate System Model, version 4. *Journal of Climate*, 25(9):3053–70, 2012.

R.B. Neale, C.-C. Chen, A. Gettelman, P.H. Lauritzen, S. Park, D.L. Williamson, A.J. Conley, R. Garcia, D. Kinnison, J.-F. Lamarque, D. Marsh, M. Mills, A.K. Smith, S. Tilmes, F. Vitt, H. Morrison, P. Cameron-Smith, W.D. Collins, W.J. Iacono, R.C. Easter, S.J. Ghan, X. Liu, P.J. Rasch, and M.A. Taylor and. Description of NCAR Community Atmosphere Model (CAM 5.0). NCAR Technical Note TN-486+STR, NCAR, Nov 2012.

E.C. Hunke and W.H. Lipscomb. CICE: the Los Alamos sea ice model, documentation and software, version 4.0. Technical Report LA-CC-06-012, Los Alamos National Laboratory, 2008.

K.W. Oleson, D.M. Lawrence, G.B. Bonan, M.G. Flanner, E. Kluzek, P.J. Lawrence, S. Levis, S.C. Swenson, P.E. Thornton, A. Dai, M. Decker, R. Dickinson, J. Feddema, C.L. Heald, F. Hoffman, J.-F. Lamarque, N. Mahowald, G.-Y. Niu, T. Qian, J. Randerson, S. Running, K. Sakaguchi, A. Slater, R. Stockli, A. Wang, Z.-L. Yang, X. Zeng, and X. Zeng. Technical description of version 4.0 of the Community Land Model (CLM). Technical Report TN-478+STR, National Center for Atmospheric Research, 2010.

Hansi Singh, Nicole Feldl, Jennifer E Kay, and Ariel L Morrison. Climate sensitivity is sensitive to changes in ocean heat transport. *Journal of Climate*, pages 1–60, 2022.

J.E. Kay, C. Deser, A. Phillips, A. Mai, C. Hannay, G. Strand, J.M. Arblaster, S.C. Bates, G. Danabasoglu, J. Edwards, M. Holland, P. Kushner, J.-F. Lamarque, D. Lawrence, K. Lindsay, A. Middleton, E. Munoz, R. Neale, K. Oleson, L. Polvani, and M. Vertenstein. The Community Earth System Model (CESM) Large Ensemble project: A community resource for studying climate change in the presence of internal climate variability. *Bulletin of the American Meteorological Society*, 96:1333–1349, 2015.

IPCC. *Climate Change 2021: The Physical Science Basis. Contribution of Working Group I to the Sixth Assessment Report of the Intergovernmental Panel on Climate Change*, volume In Press. Cambridge University Press, Cambridge, United Kingdom and New York, NY, USA, 2021. doi: 10.1017/9781009157896.

J. Bjerknes. Atlantic air-sea interaction. *Advances in Geophysics*, 10:1–82, 1964.

Len Shaffrey and Rowan Sutton. Bjerknes compensation and the decadal variability of the energy transports in a coupled climate model. *Journal of Climate*, 19 (7):1167–1181, 2006.

Riccardo Farneti and Geoffrey K Vallis. Meridional energy transport in the coupled atmosphere–ocean system: Compensation and partitioning. *Journal of climate*, 26(18):7151–7166, 2013.

Haijun Yang, Yingying Zhao, Zhengyu Liu, Qing Li, Feng He, and Qiong Zhang. Heat transport compensation in atmosphere and ocean over the past 22,000 years. *Scientific reports*, 5(1):1–11, 2015.

P.H. Stone. Constraints on dynamical transports of energy on a spherical planet. *Dynamics of Atmospheres and Oceans*, 2:123–139, 1978.

B.J. Soden, I.M. Held, R. Colman, K.M. Shell, and J.T. Kiehl. Quantifying climate feedbacks using radiative kernels. *Journal of Climate*, 21:3504–3520, 2008.

K.M. Shell, J.T. Kiehl, and C.A. Shields. Radiative kernel technique to calculate climate feedbacks in NCAR's Community Atmospheric Model. *Journal of Climate*, 21:2269–2283, May 2008.

Angeline G Pendergrass, Andrew Conley, and Francis M Vitt. Surface and top-of-atmosphere radiative feedback kernels for CESM-CAM5. *Earth System Science Data*, 10(1):317–324, 2018.

N Feldl and GH Roe. Four perspectives on climate feedbacks. *Geophysical Research Letters*, 40(15):4007–4011, 2013a.

N. Feldl and G.H. Roe. The nonlinear and nonlocal nature of climate feedbacks. *Journal of Climate*, 26:8289–8304, 2013b.

Hugues Goosse, Jennifer E Kay, Kyle C Armour, Alejandro Bodas-Salcedo, Helene Chepfer, David Docquier, Alexandra Jonko, Paul J Kushner, Olivier Lecomte, François Massonnet, et al. Quantifying climate feedbacks in polar regions. *Nature communications*, 9(1):1–13, 2018.

M. Vellinga and P. Wu. Relations between northward ocean and atmosphere energy transports in a coupled climate model. *Journal of Climate*, 21:561–575, Feb 2008.

R Sutton and P-P Mathieu. Response of the atmosphere–ocean mixed-layer system to anomalous ocean heat-flux convergence. *Quarterly Journal of the Royal Meteorological Society: A journal of the atmospheric sciences, applied meteorology and physical oceanography*, 128(582):1259–1275, 2002.

Navid C Constantinou and Andrew McC Hogg. Intrinsic oceanic decadal variability of upper-ocean heat content. *Journal of Climate*, 34(15):6175–6189, 2021.

DB Bonan, KC Armour, GH Roe, N Siler, and N Feldl. Sources of uncertainty in the meridional pattern of climate change. *Geophysical Research Letters*, 45(17): 9131–9140, 2018.

Nicholas Siler, Gerard H Roe, Kyle C Armour, and Nicole Feldl. Revisiting the surface-energy-flux perspective on the sensitivity of global precipitation to climate change. *Climate Dynamics*, 52(7):3983–3995, 2019.